Nano Research
2023, 16(6): 8433–8447

ISSN 1998-0124 CN 11-5974/O4
https://doi.org/10.1007/s12274-022-5364-5

Research Article

Current collectors based on multiwalled carbon-nanotubes and few-layer graphene for enhancing the conversion process in scalable lithium-sulfur battery

Vittorio Marangon[1,2], Edoardo Barcaro[2], Luca Minnetti[1], Wolfgang Brehm[3], Francesco Bonaccorso[1,3], Vittorio Pellegrini[1,3], and Jusef Hassoun[1,2,4] (✉)

[1] *Graphene Labs, Istituto Italiano di Tecnologia, Genoa 16163, Italy*
[2] *Department of Chemical, Pharmaceutical and Agricultural Sciences, University of Ferrara, Ferrara 44121, Italy*
[3] *BeDimensional S.p.A., Genoa 16163, Italy*
[4] *National Interuniversity Consortium of Materials Science and Technology (INSTM), University of Ferrara Research Unit, Ferrara 44121, Italy*

Received: 30 August 2022 / **Revised:** 4 November 2022 / **Accepted:** 27 November 2022

ABSTRACT

We investigated herein the morphological, structural, and electrochemical features of electrodes using a sulfur (S)-super P carbon (SPC) composite (i.e., S@SPC-73), and including few-layer graphene (FLG), multiwalled carbon nanotubes (MWCNTs), or a mixture of them within the current collector design. Furthermore, we studied the effect of two different electron-conducting agents, that is, SPC and FLG, used in the slurry for the electrode preparation. The supports have high structural crystallinity, while their morphologies are dependent on the type of material used. Cyclic voltammetry (CV) shows a reversible and stable conversion reaction between Li and S with an activation process upon the first cycle leading to the decrease of cell polarization. This activation process is verified by electrochemical impedance spectroscopy (EIS) with a decrease of the resistance after the first CV scan. Furthermore, CV at increasing scan rates indicates a Li^+ diffusion coefficient (D) ranging between 10^{-9} and 10^{-7} $cm^2 \cdot s^{-1}$ in the various states of charge of the cell, and the highest D value for the electrodes using FLG as electron-conducting agent. Galvanostatic tests performed at constant current of C/5 (1 C = 1675 $mA \cdot g_S^{-1}$) show high initial specific capacity values, which decrease during the initial cycles due to a partial loss of the active material, and subsequently increase due to the activation process. All the electrodes show a Coulombic efficiency higher than 97% upon the initial cycles, and a retention strongly dependent on the electrode formulation. Therefore, this study suggests a careful control of the electrode in terms of current collector design and slurry composition to achieve good electrode morphology, mechanical stability, and promising electrochemical performance in practical Li-S cells.

KEYWORDS

lithium-sulfur battery, current collector, few-layer graphene, carbon nanotubes, scalability, sulfur loading

1 Introduction

Lithium-sulfur (Li-S) batteries are promising electrochemical energy storage devices due to the intrinsic conversion process between Li and S, that is, $16Li + S_8 \rightleftharpoons 8Li_2S$, which delivers a theoretical energy density of 2600 $Wh \cdot kg^{-1}$ as referred to Li_2S [1–3]. Moreover, the use of the environmentally compatible and cheap sulfur is expected to greatly limit the cost of the battery compared to the lithium-ion systems using expensive and possibly toxic metals such as cobalt [1]. Massive research has been so far devoted on solving the challenges affecting this promising battery, namely, the insulant character of sulfur [3], a safe use of the reactive lithium metal, the flammable organic electrolytes [4, 5], and the uncontrolled diffusion and parasite reactions of the lithium polysulfides intermediates Li_2S_x ($2 \leq x \leq 8$) formed during the discharge process [6–8]. In fact, long-chain polysulfides such as Li_2S_8 and Li_2S_6 can dissolve in the electrolyte media, migrate through the organic solution, directly react through reduction at the Li anode surface, and diffuse back to the cathode to be newly oxidized. This undesired process named as "polysulfide shuttle" can lead to a continuous charging process without any energy storage [9, 10]. In this regard, the preparation of sulfur composites including carbons with various morphologies [11–15], conductive polymers [16–18], metals [19–21], metal–organic frameworks (MOFs) [22–24], or metal oxides [25–27] has been considered as a suitable strategy for enhancing the conductivity of the sulfur electrode and, at the same time, retaining the lithium polysulfides through chemical/physical interactions. Intensive research has also been devoted to non-flammable and stable organic solvents to design electrolytes of practical interest. Among the various alternatives, glymes ($CH_3(OCH_2CH_2)_nOCH_3$, $2 \leq n \leq 4$) [28–30], solid polymers [31, 32], and inorganic composites [33] have revealed the most promising features in Li-S cell. Furthermore, sacrificial additives such as $LiNO_3$ or sulfides [34] have been suggested to react at the lithium anode surface and form a stable protective passivation layer indicated as solid electrolyte interphase (SEI), which strongly mitigates the side reactions of the Li_2S_x

Address correspondence to jusef.hassoun@unife.it

intermediates [35, 36]. The encouraging results recently obtained have led to the refinement of suitable Li-S cell parameters to achieve practical configurations of the battery with high gravimetric and volumetric energy density. In particular, the focus was the sulfur loading on the cathode side, the amount of the conductive matrix in the sulfur bulk, and the electrolyte/sulfur (E/S) ratio [37, 38]. Following this thread, our recent works have highlighted the importance of the cathode current collector optimization to achieve a battery with enhanced performances in terms of both gravimetric and volumetric energy density [39, 40]. Hence, fibrous carbon-cloth supports such as gas diffusion layers (GDLs) allowed the infiltration of the amorphous sulfur upon charge, thus leading to improved conductivity of the cathode and to an overall enhancement of the cell electrochemical performance [39, 40]. This unique feature represented a relevant advantage of GDLs compared to conventional metallic cathode supports such as aluminum, which allow only partial sulfur utilization due to a characteristic flat surface [41]. Despite the silver linings associated with GDL-like supports, their excessive thickness (> 400 μm) compared to aluminum (~ 15 μm) can drastically affect the cell volumetric energy density and avoid an actual application in practical energy storage systems. Therefore, casting of conductive and porous carbon coatings on aluminum substrates may represent a fair compromise between efficient sulfur utilization and appropriate thickness of the cathode [42]. We have explored in a recent work the application of sulfur electrodes using a few-layer graphene (FLG)-coated aluminum support in lithium cell with notably enhanced electrochemical performance compared with the bare Al, while exhibiting an average thickness of ~ 40 μm [43]. The use of graphene-based materials in Li-S batteries has been recently considered due to its favorable properties including high electrical conductivity, large surface area, notable mechanical stability, and the ability of the oxygen-rich surface functional groups in anchoring polysulfides [44–46]. In particular, the use of FLG produced by exfoliation of graphite by wet-jet mill (WJM) process [47–48] appeared an interesting strategy for enhancing Li-S performance [49]. Multi-walled carbon nanotubes (MWCNTs) have been often included in the sulfur cathode due to their excellent conductivity and macro-porosity provided by the characteristic interwoven structure [50, 51]. The latter can allow electrolyte swelling, sulfur accommodation, polysulfides restrain, and compensation of the volume changes of the cathode during cycling [50, 51]. Therefore, various combinations between graphene and carbon nanotubes-based material have been proposed in literature as an effective strategy for enabling a high energy density Li-S battery [52, 53].

In this work, we extended the study of the above key parameters to current collectors consisting of aluminum substrates suitably coated by either FLG, MWCNTs, or a combination of them (50:50 wt.%) to optimize the Li-S battery operation. The supports were investigated in terms of morphology and structure and used in lithium cells with a composite formed by elemental sulfur including carbon black (70:30 wt.%). To further investigate the effects of the sulfur cathode composition on the lithium cell properties and electrochemical performance, two different electron conductive agents, that is, amorphous carbon black and FLG, were also used in the electrode slurry formulation. The resulting electrodes were thoroughly characterized in terms of morphology and electrochemical features in lithium cells by evaluating the reversibility, the cycling performance, and stability of the Li-S conversion process. Importantly, the Li^+ diffusional properties through the electrode/electrolyte interphase were studied. The results suggested a crucial role of the FLG in enhancing the mechanical stability of the electrode and strongly improving the Li^+ ion diffusion. Furthermore, the data indicated an optimal cycling stability of the cells combining FLG conductive agent and MWCNTs coating on the aluminum support.

2 Experimental section

2.1 Current collectors preparation

FLG (obtained by WJM process) [47–48] and MWCNTs (> 90% carbon basis, $D \times L$: 110–170 nm × 5–9 μm, Sigma-Aldrich) were chosen as carbon materials to prepare three different current collectors. Slurries composed of carbon material (90 wt.%), that is, FLG, MWCNTs, or FLG:MWCNTs 50:50 wt.% mixture, and polyvinilidene fluoride (10 wt.%, Solef 6020 PVDF) polymer binder were prepared by dispersing the components in N-methyl-2-pyrrolidone (NMP, Sigma-Aldrich) solvent. The resulting slurries were coated on aluminum foils (MTI Corp., 15 μm thick) using a doctor blade tool (MTI Corp.) and adjusting the thickness in order to achieve a carbon loading of ~ 1 mg·cm^{-2}. The coated aluminum foils were dried at 70 °C until complete evaporation of the solvent and subsequently hand roll-pressed to reduce thickness and improve the coating tap density. The obtained current collectors were indicated in the text as S7 (FLG:PVDF 90:10 wt.%), S8 (MWCNTs:PVDF 90:10 wt.%), and S9 ((FLG:MWCNTs 50:50 wt.%):PVDF 90:10 wt.%), and the acronyms are collected in Table 1 for reader's convenience. The thickness of the S7, S8, and S9 current collectors was measured using a Palmer digital thickness gauge (Table 2). The morphological features of the carbon-coated Al current collectors were investigated by scanning electron microscopy (SEM) through a Zeiss EVO MA10 microscope exploiting a tungsten thermionic electron source, while energy dispersive X-ray spectroscopy (EDS) was carried out on the SEM images by a X-ACT Cambridge Instruments analyzer. Additional investigation of the current collectors morphology was performed by transmission electron microscopy (TEM) by using a Zeiss EM 910 microscope equipped with a tungsten thermoionic electron gun operating at 100 kV. The structure of the current collectors was studied via X-ray diffraction (XRD) by performing scans between 10° and 60° (2θ) at 10 s·step^{-1} (step size of 0.02°) through a Bruker D8 Advance diffractometer exploiting a Cu-Kα source (8.05 keV).

2.2 Sulfur electrodes preparation

The sulfur-carbon composite used in cathodes for lithium cell consisted of a mixture of elemental sulfur and amorphous super P carbon (SPC, Timcal) combined by the 70:30 weight ratio through melting procedure as reported previously [54]. Accordingly, elemental sulfur (≥ 99.5 %, Riedel-de Haën) and SPC were ground together and heated at 125 °C in a silicon oil bath under continuous stirring until complete melting of sulfur and blending with SPC. Afterwards, the mixture was quenched at room temperature until solidification, and ground to achieve a fine powder. The final composite is indicated as S@SPC-73. Sulfur electrodes were prepared by doctor blade casting on the S7, S8,

Table 1 Sample acronyms[a]

Acronym	Specification
S7	(90 wt.% FLG, 10 wt.% PVDF)-coated Al support
S8	(90 wt.% MWCNTs, 10 wt.% PVDF)-coated Al support
S9	(90 wt.% (FLG:MWCNTs, 50:50 wt.%), 10 wt.% PVDF)-coated Al support
E1	SPC
E2	FLG

[a]Acronyms used to indicate the carbon-coated aluminum current collectors (S) and the electron conductive agents (E) used herein.

Table 2 Physical characteristics of the Al-coated current collectors[a]

Current collector	Thickness (μm)	Carbon loading (mg·cm^{-2})
Al	15	—
S7	40	1.3
S8	60	1.2
S9	50	1.0
GDL	454	—

[a]The data for aluminum and GDL supports are provided by MTI Corporation.

and S9 current collectors of slurries combining S@SPC-73, a carbon electron conductive agent, and the PVDF polymer binder by the 80:10:10 weight ratio through dispersion in NMP solvent. Two different carbon electron conductive agents were used, i.e., either SPC or FLG, indicated as E1 and E2, respectively, when cited in cell or electrode configurations. The acronyms are also collected in Table 1 for reader's convenience. The six electrode foils obtained by combining the S@SPC-73_E1 and S@SPC-73_E2 formulations with the S7, S8, and S9 current collectors were dried on a hot plate at 50 °C for 3 h to remove the NMP solvent. Subsequently, the electrode foils were hand roll-pressed and cut into 14 mm-diameter disks (1.54 cm^2 geometric area) before being dried under vacuum overnight at 35 °C and transferred inside an Ar-filled glovebox (MBraun, oxygen and water levels < 1 ppm). The electrodes morphology was evaluated by SEM-EDS investigation via a Zeiss EVO MA10 microscope exploiting a tungsten thermionic electron source and a X-ACT Cambridge Instruments analyzer, respectively.

2.3 Electrochemical tests

CR2032 coin-type cells were assembled by stacking a S@SPC-73 electrode, a 16 mm-diameter Celgard 2400 separator soaked with the electrolyte, and a 14 mm-diameter lithium disk as the anode. The electrolyte solvent was prepared by mixing 1,3-dioxolane (DOL, anhydrous, containing ca. 75 ppm BHT as inhibitor, 99.8%, Sigma-Aldrich) and 1,2-dimethoxyethane (DME, anhydrous, 99.5%, inhibitor-free, Sigma-Aldrich) with 1:1 weight ratio. Then, lithium bis(trifluoromethanesulfonyl)imide ($LiN(SO_2)_2(CF_3)_2$, LiTFSI, 99.95% trace metals basis, Sigma-Aldrich) and lithium nitrate ($LiNO_3$, 99.99% trace metals basis, Sigma-Aldrich) were dissolved as conductive salt and sacrificial agent, respectively, in the solvent mixture to achieve a concentration of 1 mol for both salts in 1 kg of solvent. The electrolyte is subsequently indicated as DOL:DME, 1m LiTFSI, 1m $LiNO_3$. Before employment, DOL and DME solvents were dried under molecular sieves (rods, 3 Å, size 1/16 in., Honeywell Fluka) to ensure a water content lower than 10 ppm as verified via a Karl Fischer 899 Coulometer (Metrohm), while lithium salts were dried under vacuum for 2 days at 110 °C. The subsequent electrochemical measurements were performed on Li|S@SPC-73 cells using cathodes with a sulfur loading of ~ 2 mg·cm^{-2} and an E/S ratio of 15 μL·mg^{-1}. Cyclic voltammetry (CV) was performed at the constant scan rate of 0.1 mV·s^{-1} within the 1.8–2.8 V vs. Li^+/Li potential range, while electrochemical impedance spectroscopy (EIS) was carried out at the open circuit voltage (OCV) condition and during CV upon the 1st, 5th, and 10th cycle by applying an alternate voltage signal of 10 mV in the frequency range from 500 kHz to 100 mHz. The resulting Nyquist plots were fitted by using the non-linear least-squares (NLLS) method with the aid of the Boukamp software and only fits with a χ^2 value of the order of 10^{-4} or lower were accepted [55, 56]. CV measurements were performed at increasing scan rates, that is, 0.05, 0.1, 0.15, 0.2, and 0.25 mV·s^{-1} in the 1.8–2.8 V vs. Li^+/Li potential range to determine the Li^+ diffusion coefficient (D) by using the Randles–Sevcik equation (Eq. (1)) [57, 58]

$$I_p = 0.4463\, zFAC_{Li}(zFvD/RT)^{0.5} \quad (1)$$

where I_p is the peak current related to the potential signals recorded by CV, z is the number of exchanged electrons (z = 1 for each single discharge peak at 2.25 and 1.95 V vs. Li^+/Li, z = 2 for the broad double charge peak at 2.50 V vs. Li^+/Li), F is the Faraday constant (96,485 C·mol^{-1}), A is the electrode geometric area (1.54 cm^2), C is the estimated concentration of Li^+ in the sulfur electrode volume (mol·dm^{-3}), v is the CV scan rate (mV·s^{-1}), R is gas constant (8.31451 J·mol^{-1}·K^{-1}), and T is the room temperature (298 K). CV and EIS tests were carried out by using a VersaSTAT MC Princeton Applied Research (PAR-AMETEK) instrument at room temperature (25 °C). Li|S@SPC-73 cells were galvanostatically cycled at the constant current rate of C/5 (1 C = 1675 mA·g^{-1}) between 1.9 and 2.8 V through a MACCOR series 4000 battery test system at room temperature (25 °C).

Additional discharge/charge cycles were performed on Li|S@SPC-73_E2_S8 cells using either a cathode sulfur loading of 5 mg·cm^{-2} and an E/S ratio of 10 μL·mg^{-1}, or a sulfur loading of 6.5 mg·cm^{-2} with an E/S ratio of 7 μL·mg^{-1}. The cells were cycled at the constant current rate of either C/5 or C/10, respectively, within the 1.7–2.8 V voltage range in a chamber with a controlled temperature of 30 °C with a maximum fluctuation of ±0.1 °C with respect to the set-point.

3 Results and discussion

3.1 Current collectors investigation

The morphological and structural features of the carbon-coated Al current collectors using either FLG, MWCNTs, or the FLG:MWCNTs 50:50 wt.% (S7, S8, and S9, respectively, in Table 1) are reported in Fig. 1 by SEM-EDS (images in Figs. 1(a)–1(r)) and XRD (patterns in Figs. 1(s)–1(u)). The data recorded for the S7 (Figs. 1(a)–1(f) and 1(s)), S8 (Figs. 1(g)–1(l) and 1(t)), and S9 (Figs. 1(m)–1(r) and 1(u)) show substantial differences in terms of carbon particle distribution and shape at the current collector surface as well as of crystallinity. In particular, the SEM of S7 (Figs. 1(a)–1(c)) clearly evidences the presence of FLG flakes with dimensions > 1 μm leading to a uniform coating in which the C (EDS in Fig. 1(d)) and the F accounting for the PVDF binding agent (EDS in Fig. 1(e)) cover the Al (EDS in Fig. 1(f)) surface. The morphology of S8 is strongly influenced by the disordered nature of the MWCNTs that leads to a porous carbon surface (Figs. 1(g)–1(i)), as also evidenced by the EDS elemental maps of C (Fig. 1(j)), F (Fig. 1(k)), and Al (Fig. 1(l)). The combination of FLG and MWCNTs in the S9 current collector is reflected into a characteristic carbon coating (Figs. 1(m)–1(o)) in which a predominant FLG-MWCNTs uniform layer and clusters formed by MWCNTs and PVDF (see EDS elemental maps in Figs. 1(p)–1(r)) are interspersed onto the Al surface. The difference between the supports in terms of crystallinity is clearly evidenced by the XRD measurements performed on S7 (Fig. 1(s)), S8 (Fig. 1(t)), and S9 (Fig. 1(u)). The current collectors containing FLG (i.e., S7 and S9) display a narrow and intense peak at ~ 2θ = 26° typical of graphitic structures due to the compact packing of the FLG layers promoted by the experimental conditions adopted herein [59], while S8 shows a broader and less intense signal characteristic of the MWCNTs structure [54]. The substantially lower crystallinity due to MWCNTs compared to FLG in the current collectors can influence the performance of Li-S batteries. The use of low crystalline porous carbon collectors, such as the GDL, has already evidenced crucial improvements compared to the conventional flat Al [39–41]. In fact, GDL can efficiently host the elemental sulfur formed during charge into the widely

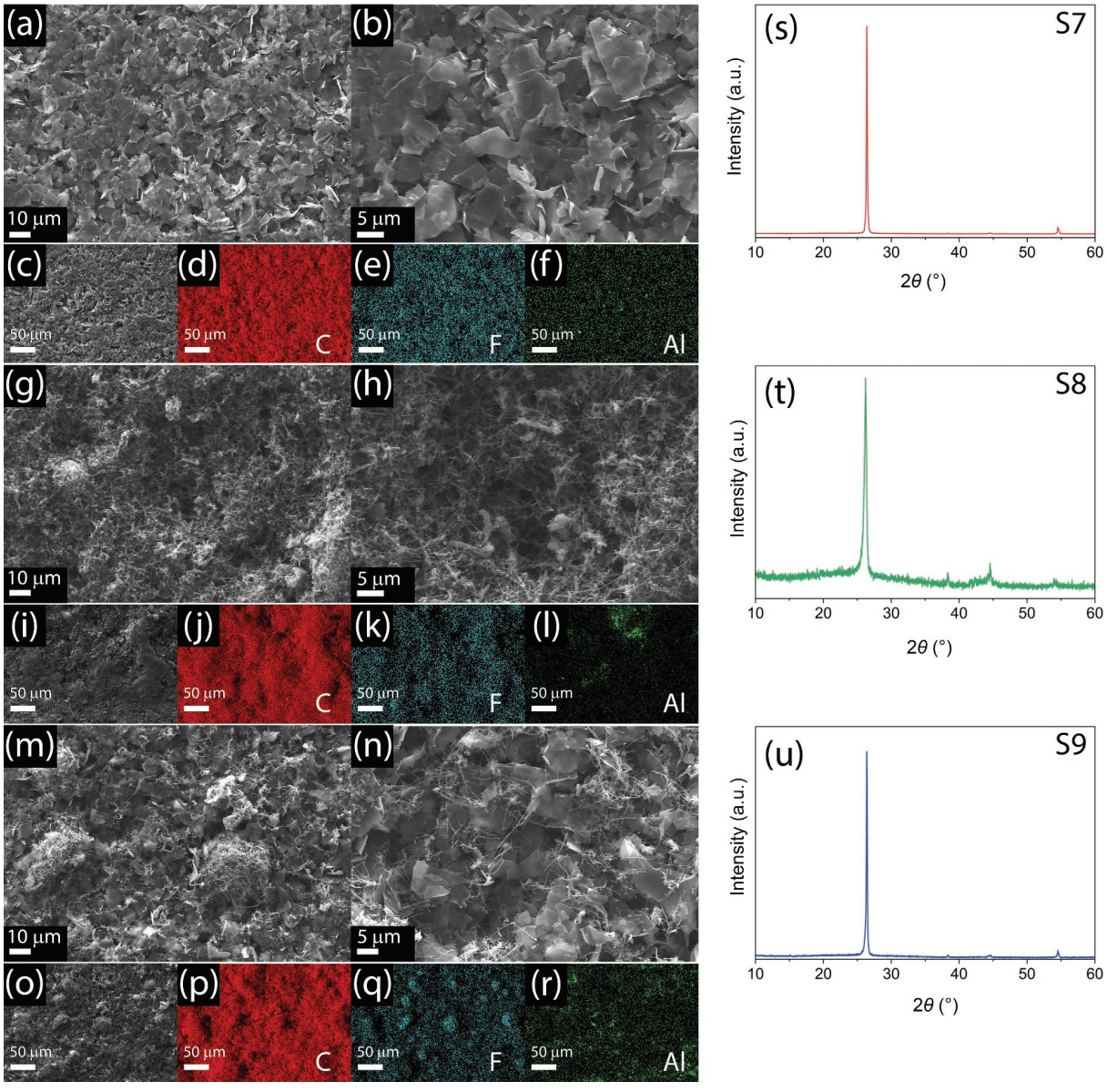

Figure 1 SEM-EDS analyses of the (a)–(f) S7, (g)–(l) S8, and (m)–(r) S9 carbon-coated aluminum current collectors; in detail: (a)–(c), (g)–(i), and (m)–(o) SEM images at various magnifications, and (d)–(f), (j)–(l), and (p)–(r) corresponding EDS elemental maps of ((d), (j), and (p)) C, ((e), (k), and (q)) F, and ((f), (l), and (r)) Al. X-ray diffractograms of the (s) S7, (t) S8, and (u) S9 carbon-coated aluminum current collectors. See the Experimental section and Table 1 for acronyms.

available space in the support structure, thus enhancing the electric contact of the active material with the electrode and improving the battery performance [39–41]. Therefore, MWCNTs could in principle ensure a suitable porosity of the carbon coating due to the wide spatial distribution of the nanotubes and allow sulfur infiltration [60], whereas the packed FLG flakes may provide mechanical robustness and flexibility [61]. Previous literature suggested the combination of MWCNTs and FLG as an optimal carbon framework having remarkable porosity and stability, allowing efficient sulfur operation in lithium battery [52, 62]. In this framework, the replacement of thick carbon current collectors such as GDL with carbon-coated aluminum supports actually represents a key factor to achieve Li-S batteries with volumetric energy density of practical interest.

According to the data reported in Table 2, GDL support has a thickness as high as 454 μm, conventional aluminum exhibits a value limited to 15 μm, whilst S7, S8, and S9 carbon-coated aluminum current collectors with carbon loading of ~ 1 mg·cm^{-2} exhibit thicknesses of 40, 60, and 50 μm, respectively, which are considered an adequate compromise for practical applicability and enhanced performance in Li-S cell.

Further insights on the morphology of the S7, S8, and S9 supports are provided by TEM images in Fig. 2 which were carried out on carbon:PVDF samples scratched out from the coated-aluminum foils. The micrographs well display the presence of stacked micrometric flakes of FLG in S7 (Figs. 2(a) and 2(b)), and the formation of almost aligned MWCNTs with a length exceeding 1 μm and a diameter approaching 100 nm in S8 (Figs. 2(c) and 2(d)). Instead, the mixed sample S9 shows the characteristic formation of a composite morphology determined by the concomitant presence of FLG, MWCNTs, and PVDF. Interestingly, the TEM images in Fig. 2 depict with a magnified detail the same outcomes of the SEM-EDS evidenced in Fig. 1, and account for a substantial difference between the various supports depending on the carbon nature, which is expected to control the sulfur electrode characteristics.

3.2 Sulfur electrodes characterization

The S@SPC-73 composite was chosen to prepare sulfur electrodes for lithium batteries using the S7, S8, and S9 current collectors, and either SPC (E1) or FLG (E2) conductive agents (see the Experimental section and Table 1 for acronyms). The resulting six

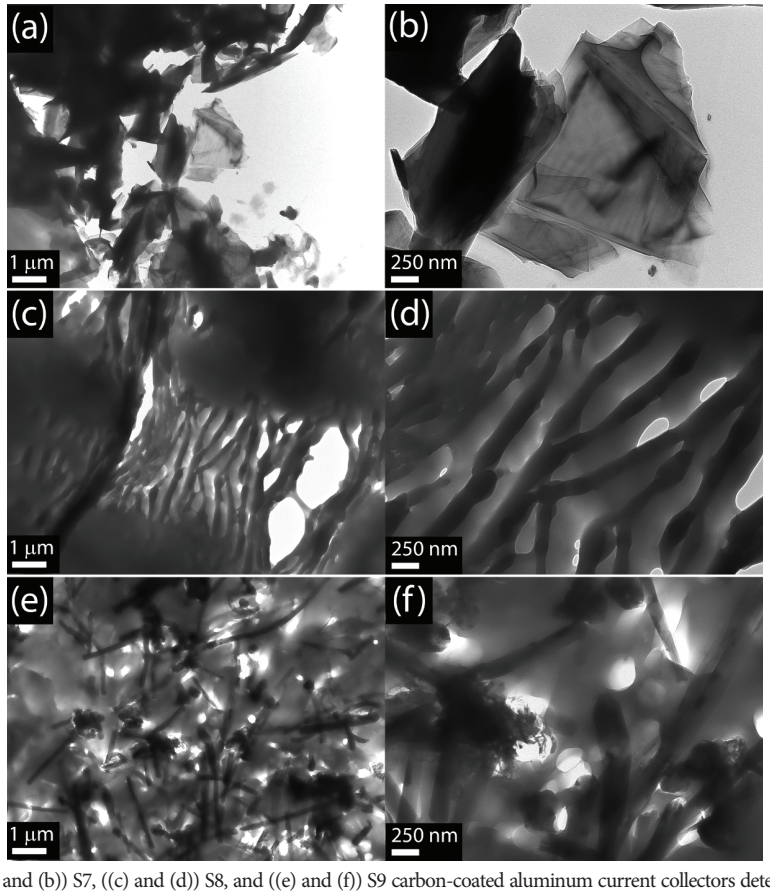

Figure 2 TEM images of the ((a) and (b)) S7, ((c) and (d)) S8, and ((e) and (f)) S9 carbon-coated aluminum current collectors detected at various magnification. The measurements were performed on carbon:PVDF samples scratched out form the various coated-aluminum foils. See the Experimental section and Table 1 for acronyms.

cathodes were studied through SEM-EDS measurements, as reported in Figs. S1 and S2 in the Electronic Supplementary Material (ESM) for the S@SPC-73_E1 and S@SPC-73_E2, respectively. The S@SPC-73_E1 cathodes show a uniform distribution of amorphous SPC and sulfur in the electrode film either using S7 (Figs. S1(a)–S1(c) in the ESM), S8 (Figs. S1(d)–S1(f) in the ESM), or S9 (Figs. S1(g)–S1(i) in the ESM), as evidenced by the C and S EDS elemental maps in the right-hand insets of Figs. S1(a), S1(d), and S1(g) in the ESM. The electrodes clearly display micrometric fractures extended to the current collector surface. The presence of these fractures is strongly limited by using the FLG electron conductive agent instead of SPC, as demonstrated for the S@SPC-73_E2 electrodes in Fig. S2 in the ESM. In fact, the cathodes using S7 (Figs. S2(a)–S2(c) in the ESM), S8 (Figs. S2(d)–S2(f) in the ESM), and S9 (Figs. S2(g)–S2(i) in the ESM) exhibit a uniform surface in which S@SPC-73 composite is blended with the FLG flakes without relevant micrometric fractures, and uninterrupted distribution across the films of C and S in the corresponding EDS elemental maps (right-hand insets of Figs. S2(a), S2(d), and S2(g) in the ESM). This key difference is reflected into a notable mechanical stability observed for the layers using FLG compared to the amorphous SPC as conductive agent. However, the higher porosity of the S@SPC-73_E1 cathode films may allow a better sulfur rearrangement during Li-S cell charge, and higher capacity values.

The Li-S electrochemical conversion process of the prepared electrodes was hereafter investigated by CV and the evolution of the electrode/electrolyte interphase by EIS upon CV. Figure 3 reports the results of the CV (Figs. 3(a), 3(c), and 3(e)) and the EIS (Figs. 3(b), 3(d), and 3(f)) tests related to S@SPC-73_E1 electrodes using the S7 (Figs. 3(a) and 3(b)), S8 (Figs. 3(c) and 3(d)), and S9 (Figs. 3(e) and 3(f)) current collectors (see Table 1 in the Experimental section for acronyms). All the above voltammograms reveal during the first cycle the typical evolution of the Li-S conversion, characterized by two reduction peaks at ~ 2.20 and ~ 1.95 V vs. Li^+/Li, and by a convoluted double oxidation wave extending from 2.20 to 2.50 V vs. Li^+/Li. The well-defined reduction and oxidation signals during the subsequent cycles indicate reversible conversion of Li and S to Li_2S_x polysulfides ($2 \leq x \leq 8$) during discharge and the reverse formation of Li and S during charge [63]. Notably, the CV profiles of the S@SPC-73_E1 electrodes show after the first cycle a polarization decrease of the reduction peak at 2.20 V vs. Li^+/Li that shifts to slightly higher potential values. This phenomenon, usually indicated as electrochemical activation process, is associated with the stabilization of the electrode/electrolyte interphase upon the deposition of amorphous sulfur into the carbon electrode structure during charge, and the formation of a suitable SEI at the electrodes surface [39, 64, 65]. This favorable process, already observed on thick and highly porous carbon current collectors such as GDL [39, 40], suggests that the thin carbon-coated Al supports ad hoc designed herein can actually be used in advanced Li-S prototype with satisfactory volumetric energy density [43]. Interestingly, the CV of the various Li|S@SPC-73_E1 cells evidence slight differences in the peak width and intensity. In particular, the voltammogram related to the S@SPC-73_E1_S8 electrode (Fig. 3(c)) displays during the first cycle broader peaks and less intense reduction signal at 1.95 V vs. Li^+/Li with respect to the S@SPC-73_E1 electrodes using S7 (Fig. 3(a)) and S9 (Fig. 3(e)).

Meanwhile, the S@SPC-73_E1_S8 oxidation double-signal gradually reduces in width during subsequent cycles, and the current intensity of the 1.95 V vs. Li^+/Li peak increases concomitantly. On the other hand, the S@SPC-73_E1_S9 electrode (Fig. 3(e)) delivers the sharpest and most overlapped

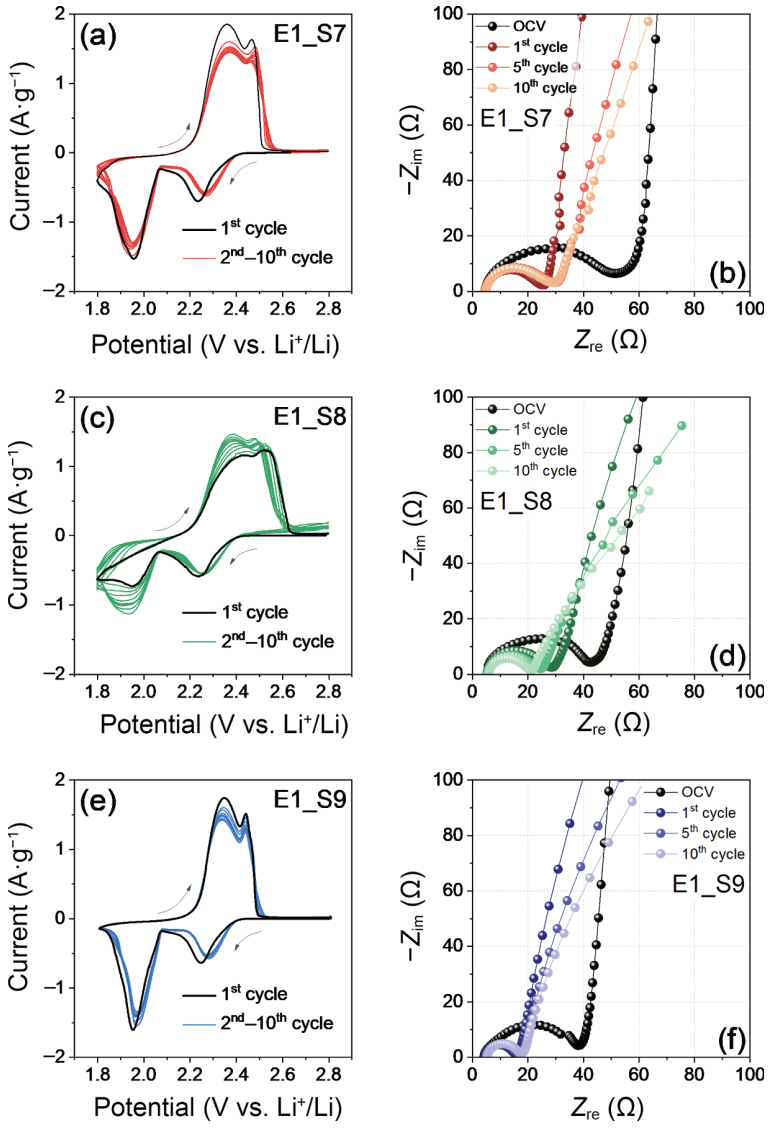

Figure 3 ((a), (c), and (e)) CV and ((b), (d), and (f)) EIS measurements performed on Li|DOL:DME, 1 m LiTFSI, 1 m $LiNO_3$|S@SPC-73_E1 cells with either the ((a) and (b)) S7, ((c) and (d)) S8, or ((e) and (f)) S9 carbon-coated Al current collectors (insets describe the various cathode combinations). Potential range: 1.8–2.8 V vs. Li^+/Li; scan rate: 0.1 mV·s^{-1}. EIS at the OCV cell condition and upon CV after the 1st, 5th, and 10th cycle between 500 kHz and 0.1 Hz; voltage signal: 10 mV. Cathode sulfur loading: 2 mg·cm^{-2} (electrode geometric area: 1.54 cm^2); E/S ratio: 15 μL·mg^{-1}. Tests performed at room temperature (25 °C). See the Experimental section and Table 1 for acronyms.

potential signals. These discrepancies suggest that the electrode film-current collector combination substantially influences the Li-S conversion kinetics, which is in turn expected to affect the battery performance. These differences are reflected by the EIS tests reported in Figs. 3(b), 3(d), and 3(f), related to the Li|S@SPC-73_E1 cells with the S7 (Fig. 3(b)), S8 (Fig. 3(d)), and S9 (Fig. 3(f)) current collectors. The resulting Nyquist plots reveal for the cells a remarkable variation of the electrode/electrolyte interphase upon CV cycling, which are quantitatively evaluated by NLLS analyses [55, 56] and reported in Table 3.

The analysis allows the description of the Nyquist plots through equivalent circuits consisting of various components including: (i) the electrolyte resistance (R_e) detected as the high-frequency intercept of the plot, (ii) a series of (R_iQ_i) elements formed by R_i resistances arranged in parallel with Q_i constant phase elements (CPEs), accounting for the electrode/electrolyte interphase with an overall resistance determined by the width of the medium-frequency convoluted semicircles as ΣR_i, (iii) an additional (R_wQ_w) element representing the semi-finite Warburg-type Li^+ diffusion displayed as low-frequency semicircle, and (iv) a final titled line representing the cell geometric capacitance [55, 56]. The Nyquist plots of the three S@SPC-73_E1 cells clearly show the effects of the above described activation process on stabilizing the electrode/electrolyte interphase. Hence, the EIS response substantially modifies as revealed by the increase of the number of (R_iQ_i) elements in the corresponding equivalent circuits, and the overall resistance (ΣR_i) decreases from values between 30 and 40 Ω at the OCV cell condition to 25 Ω for S7 (Fig. 3(b)), 16 Ω for S8 (Fig. 3(d)), and 14 Ω for S9 (Fig. 3(f)) after 10 CV scans (see Table 3) [66]. Interestingly, since from OCV the S@SPC-73_E1_S9 cell is well fitted by an equivalent circuit containing an additional (R_iQ_i) element and exhibits lower electrode/electrolyte resistance (slightly over 30 Ω) with respect to S7 and S8, whilst the S@SPC-73_E1_S7 system presents the highest resistance values (see Table 3). This difference as well as a relatively fast activation of the Li-S conversion kinetics likely suggests the combination of S@SPC-73_E1 film with the S9 current collector a possible electrode configuration for battery application. The same investigation depicted in Fig. 3 for Li cells using S@SPC-73_E1 electrode configuration is carried out in Fig. 4 for those with the S@SPC-73_E2 one, where the FLG conductive agent is used instead of SPC in the electrode films (see Table 1 for acronyms).

The corresponding CV measurements are shown in Figs. 4(a), 4(c), and 4(e) for the sulfur cathodes using the S7, S8, and S9

Table 3 NLLS analyses of Li|S@SPC-73_E1 cells[a]

Electrode	Cell condition	Circuit	R_1 (Ω)	R_2 (Ω)	$R_1 + R_2$ (Ω)	χ^2
S@SPC-73_E1_S7	OCV	$R_e(R_1Q_1)(R_wQ_w)Q_g$	41 ± 4	—	41 ± 4	8×10^{-4}
	1 CV cycle	$R_e(R_1Q_1)(R_2Q_2)Q_w$	16 ± 2	6.4 ± 2.1	22.4 ± 4.1	3×10^{-4}
	5 CV cycles	$R_e(R_1Q_1)(R_2Q_2)Q_w$	17 ± 3	9.7 ± 3.3	26.7 ± 6.3	6×10^{-4}
	10 CV cycles	$R_e(R_1Q_1)(R_2Q_2)Q_w$	17 ± 2	8.4 ± 2.3	25.4 ± 4.3	2×10^{-4}
S@SPC-73_E1_S8	OCV	$R_e(R_1Q_1)(R_wQ_w)Q_g$	40 ± 1	—	40 ± 1	1×10^{-4}
	1 CV cycle	$R_e(R_1Q_1)(R_2Q_2)Q_w$	17 ± 3	7.6 ± 3.7	24.6 ± 6.7	3×10^{-4}
	5 CV cycles	$R_e(R_1Q_1)(R_2Q_2)Q_w$	13 ± 2	5.8 ± 2.4	18.8 ± 6.6	2×10^{-4}
	10 CV cycles	$R_e(R_1Q_1)(R_2Q_2)Q_w$	12 ± 2	3.6 ± 1.6	15.6 ± 3.6	1×10^{-4}
S@SPC-73_E1_S9	OCV	$R_e(R_1Q_1)(R_2Q_2)(R_wQ_w)Q_g$	3.4 ± 1.4	30 ± 4	33.4 ± 5.4	4×10^{-4}
	1 CV cycle	$R_e(R_1Q_1)(R_2Q_2)Q_w$	9.5 ± 0.7	3.3 ± 1.0	12.8 ± 1.7	1×10^{-4}
	5 CV cycles	$R_e(R_1Q_1)(R_2Q_2)Q_w$	10 ± 1	3.2 ± 0.8	13.2 ± 1.8	7×10^{-5}
	10 CV cycles	$R_e(R_1Q_1)(R_2Q_2)Q_w$	11 ± 1	2.6 ± 0.9	13.6 ± 1.9	5×10^{-5}

[a]NLLS analyses carried out on the Nyquist plots displayed in Fig. 3 with a Boukamp software [55, 56] by exclusively accepting fits with χ^2 values of the order of 10^{-4} or lower. See the Experimental section and Table 1 for acronyms.

current collectors, respectively, while the Nyquist plots obtained through EIS upon voltammetry are displayed in Figs. 4(b), 4(d), and 4(f).

As already observed for the S@SPC-73_E1 cells, the CV responses of the S@SPC-73_E2 cells reflect a notable reversibility of the Li-S conversion process, and show two individual reduction peaks at 2.25 and 1.95 V vs. Li^+/Li reversed into a merged double wave from 2.20 to 2.45 V vs. Li^+/Li during oxidation, accounting for the formation of Li_2S_x species ($2 \le x \le 8$) and their subsequent conversion back to Li and S, respectively [63]. The voltammograms also show the potential profiles shape improvement, the shift of the reduction peaks towards higher potentials, and the consequent polarization decrease upon the first cycle due to the activation process [39, 64, 65]. On the other hand, the voltammograms of the Li|S@SPC-73_E2 cells display better overlapping of the potential profiles and less current decrease after the first cycle with respect to the Li|S@SPC-73_E1 ones, thus suggesting an enhanced stability of the electrochemical process by using FLG in the electrode slurry [51, 67]. This experimental evidence may be ascribed to a mitigated active material loss due to the more uniform surfaces and the less extent of fractures observed through SEM-EDS for the S@SPC-73_E2 (Fig. S2 in the ESM) with respect to the S@SPC-73_E1 (Fig. S1 in the ESM). The EIS measurements performed upon CV on the Li|S@SPC-73_E2 cells displayed in Figs. 4(b), 4(d), and 4(f) for S7, S8, and S9, respectively, provide additional information on the kinetics of the Li-S conversion process. Once more, the NLLS analyses reported in Table 4 and carried out on the Nyquist plots of Fig. 4 confirm the activation upon CV, indicated by the shrink of the electrode/electrolyte interphase resistance from values of ~ 70, 60, and 40 Ω for S7 (Fig. 4(b)), S8 (Fig. 4(d)), and S9 (Fig. 4(f)) at the OCV to 30, 17, and 19 Ω after 10 CV runs, respectively [55, 56]. Despite the remarkably low electrode/electrolyte resistance achieved upon cycling, the S@SPC-73_E2 systems show slightly higher values than the respective S@SPC-73_E1 ones (comparing NLLS analyses in Tables 3 and 4). Indeed, the S@SPC-73_E1 cathodes may benefit from the higher dispersion degree of SPC amorphous powder that likely ensures a more uniform electron pathway throughout the electrode film with respect to the packed micrometric layers of FLG (Fig. 1) [39]. This hypothesis is supported by the highest electrode/electrolyte interphase resistance revealed among the various combinations for the S@SPC-73_E2_S7 system, which uses FLG both as electron conductive agent and as the only carbon coating on the Al current collector (comparing data in Tables 3 and 4). On the other hand, the remarkable mechanical stability observed for the S@SPC-73_E2 electrode set may account for a more practical use in Li-S cells, in spite of the higher resistance.

The influence of the various current collectors and electron conductive agents on the Li-S systems was further investigated by estimating the Li^+ diffusion coefficient (D) in the electrode/electrolyte interphase through Randles–Sevcik equation (see Eq. (1) in the Experimental section) [57, 58]. The CV measurements at increasing scan rates displayed in Fig. 5 were carried out on Li|S@SPC-73_E1 (Figs. 5(a)–5(c)) and Li|S@SPC-73_E2 (Figs. 5(d)–5(f)) cells with either the S7 (Figs. 5(a) and 5(d)), S8 (Figs. 5(b) and 5(e)), or S9 (Figs. 5(c) and 5(f)) current collectors. The related voltammograms reflect the signature of the Li-S conversion process observed in Figs. 3 and 4 with differences depending on the used current collector and the electron conductive agent, and show the expected increase of the current peak intensity (I_p) and the overpotential by raising the scan rate (see the Experimental section for details). The I_p of the selected reduction and oxidation signals (see inset labels in Fig. 5) are plotted vs. the square root of the scan rate ($v^{1/2}$) in Fig. S3 in the ESM to obtain the corresponding $I_p/v^{1/2}$ slope by linear fit and calculate the D value (Eq. (1)) [57, 58] for all the considered states of charge (SOC). The estimated D is reported in Table 5 and graphically represented in Fig. S4 in the ESM. As expected, different D coefficients are obtained depending on the sulfur cathode configuration, while all the electrode formulations show similar D trends throughout the CV scans. In particular, the Li-S systems exhibit the highest coefficient in the first reduction step at 2.25 V vs. Li^+/Li, i.e., between 5.9×10^{-8} and 2.3×10^{-7} $cm^2 \cdot s^{-1}$, that decreases to value between 6.9×10^{-9} and 1.3×10^{-7} $cm^2 \cdot s^{-1}$ in the subsequent discharge step at 1.95 V vs. Li^+/Li (Table 5). This trend is coherent with the prevalent presence of soluble long-chain polysulfides such as Li_2S_8 and Li_2S_6 during the initial discharge step at 2.25 V vs. Li^+/Li characterized by high ionic mobility which allows fast diffusion of the Li^+, subsequently hindered by the abundance of the solid insulating short-chain polysulfides (Li_2S_x, $1 \le x \le 4$) achieved with the ongoing of the discharge at 1.95 V vs. Li^+/Li [39]. Interestingly, a different trend of the D coefficient upon charge is observed for the various sulfur electrodes (Fig. S4 in the ESM). The electrodes using E1 (Figs. S4(a)–S4(c) in the ESM) and the E2_S8 configuration (Fig. S4(e) in the ESM) exhibit a slight increase of the D value upon charge occurring at 2.50 V vs. Li^+/Li. On the other hand, the electrodes using the E2_S7 (Fig. S4(d) in

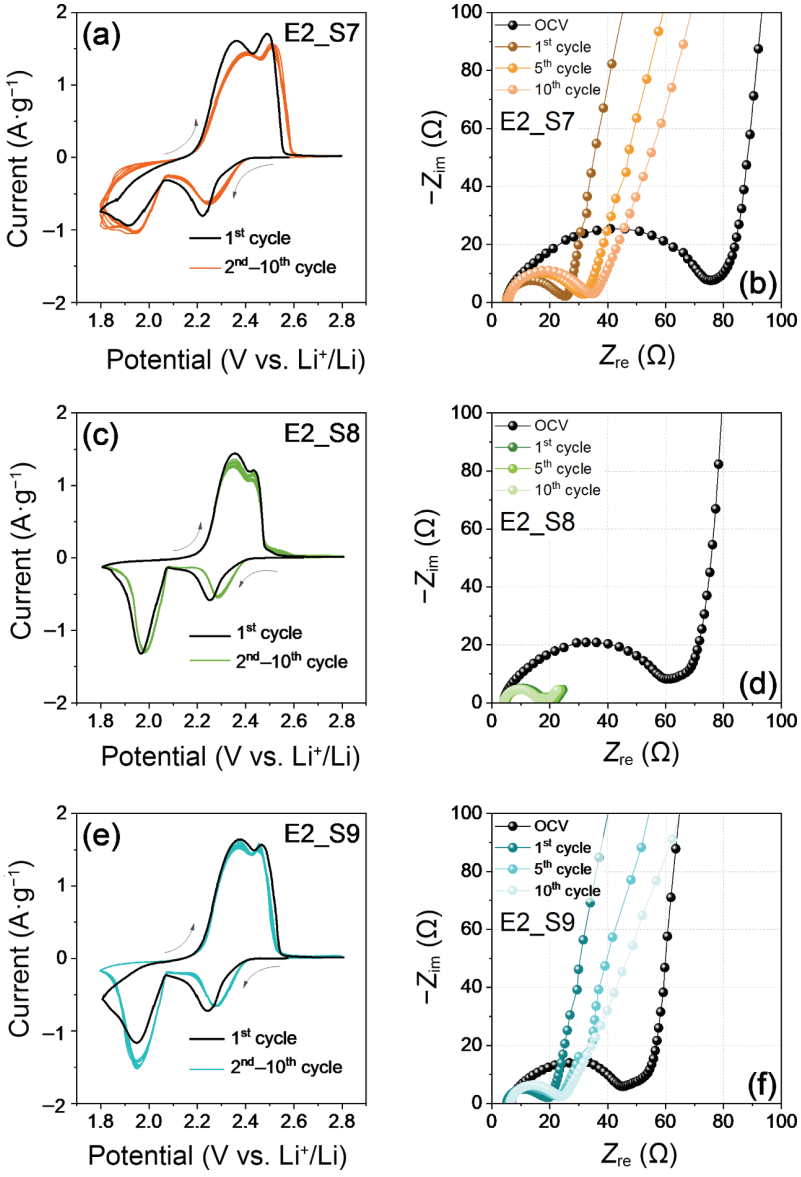

Figure 4 ((a), (c), and (e)) CV and ((b), (d), and (f)) EIS measurements performed on Li|DOL:DME, 1 m LiTFSI, 1 m $LiNO_3$|S@SPC-73_E2 cells with either the ((a) and (b)) S7, ((c) and (d)) S8, or ((e) and (f)) S9 carbon-coated Al current collectors (insets describe the various cathode combinations). Potential range: 1.8–2.8 V vs. Li^+/Li; scan rate: 0.1 mV·s^{-1}. EIS at the OCV cell condition and upon CV after the 1st, 5th, and 10th cycle between 500 kHz and 0.1 Hz; and voltage signal: 10 mV. Cathode sulfur loading: 2 mg·cm^{-2} (electrode geometric area: 1.54 cm^2); E/S ratio: 15 µL·mg^{-1}. Room temperature (25 °C). See the Experimental section and Table 1 for acronyms.

the ESM) and E2_S9 (Fig. S4(f) in the ESM) combinations are the only ones with a slight decrease upon oxidation. As previously mentioned for the resistance trends (see Fig. 4 discussion), this interesting aspect may be due to the concomitant use of FLG both as the electron conductive agent (E2) and as carbon coating on the aluminum current collector (S7) in the S@SPC-73_E2_S7 electrode that can partially limit the diffusion pathway on the electrode/electrolyte interphase upon the deposition of amorphous sulfur during charge, although further studies are certainly required to confirm this hypothesis. Nevertheless, the S@SPC-73_E2_S9 electrode shows the highest *D* coefficient with values ranging between 2.3×10^{-7} and 1.1×10^{-7} $cm^2 \cdot s^{-1}$ (see Table 5), and well matches the results obtained using the same evaluation method for sulfur electrodes exploiting highly conductive porous carbon current collectors [39, 40, 51, 68]. Relevantly, all S@SPC-73 electrodes provide *D* values of the order of 10^{-8}–10^{-7} $cm^2 \cdot s^{-1}$, except for S@SPC-73_E1_S7 (Fig. S4(a) in the ESM) that shows the lowest values of 6.9×10^{-9}–5.9×10^{-8} $cm^2 \cdot s^{-1}$, likely due to unfavorable kinetics related to the materials combination, which may need additional investigations. Beneficial effects on the Li^+ diffusion may derive from the use of MWCNTs in the support due to the increased porosity compared to the flat FLG (see Fig. 1 and Table 2). This feature likely leads to better electrode/electrolyte contact and enhanced hosting ability of the solution in the electrode. However, further studies are required to fully clarify the actual role of the various components on the diffusional features of the electrode.

Galvanostatic discharge/charge cycling tests were carried out hereafter at the constant current rate of C/5 (1 C = 1675 mA·g^{-1}) on Li|S@SPC-73 cells exploiting a sulfur loading of ~ 2 mg·cm^{-2} (electrode geometric area of 1.54 cm^2) and an E/S ratio of 15 µL·mg_S^{-1}. These relatively mild parameters are preliminarily chosen in order to achieve the best performance of the various sulfur electrodes, and to compare the obtained results with literature reports on Li-S battery [39, 40]. Figure 6 shows the voltage profiles (Figs. 6(a), 6(c), and 6(e)) and capacity trends (Figs. 6(b), 6(d), and 6(f)) of lithium cells using S@SPC-73_E1 electrodes with either the S7 (Figs. 6(a) and 6(b)), S8 (Figs. 6(c) and 6(d)), or S9 (Figs. 6(e) and 6(f)) current collectors. The selected voltage profiles (Figs. 6(a), 6(c), and 6(e)) reveal for all the cells the evolution of the double-step Li-S conversion process identified by two discharge plateaus at ~ 2.3 and ~ 2.1 V reversed

Table 4 NLLS analyses of Li|S@SPC-73_E2 cells[a]

Electrode	Cell condition	Circuit	R_1 (Ω)	R_2 (Ω)	$R_1 + R_2$ (Ω)	χ^2
S@SPC-73_E2_S7	OCV	$R_e(R_1Q_1)(R_wQ_w)Q_g$	74 ± 1	—	74 ± 1	4×10^{-4}
	1 CV cycle	$R_e(R_1Q_1)(R_2Q_2)Q_w$	15 ± 2	6.3 ± 1.8	21.3 ± 3.8	3×10^{-4}
	5 CV cycles	$R_e(R_1Q_1)(R_2Q_2)Q_w$	20 ± 2	7.6 ± 1.9	27.6 ± 3.9	4×10^{-5}
	10 CV cycles	$R_e(R_1Q_1)(R_2Q_2)Q_w$	22 ± 2	8.3 ± 1.9	30.3 ± 3.9	2×10^{-4}
S@SPC-73_E2_S8	OCV	$R_e(R_1Q_1)(R_wQ_w)Q_g$	58 ± 1	—	58 ± 1	5×10^{-4}
	1 CV cycle	$R_e(R_1Q_1)(R_2Q_2)Q_w$	9.9 ± 0.5	4.8 ± 0.8	14.7 ± 1.3	3×10^{-4}
	5 CV cycles	$R_e(R_1Q_1)(R_2Q_2)Q_w$	10 ± 0.4	6.3 ± 0.6	16.3 ± 1	2×10^{-4}
	10 CV cycles	$R_e(R_1Q_1)(R_2Q_2)Q_w$	11 ± 0.4	6.3 ± 0.6	17.3 ± 1	2×10^{-4}
S@SPC-73_E2_S9	OCV	$R_e(R_1Q_1)(R_wQ_w)Q_g$	40 ± 0.2	–	40 ± 0.2	4×10^{-4}
	1 CV cycle	$R_e(R_1Q_1)(R_2Q_2)Q_w$	9.3 ± 1.3	7.0 ± 1.6	16.3 ± 2.9	9×10^{-5}
	5 CV cycles	$R_e(R_1Q_1)(R_2Q_2)Q_w$	11 ± 1	7.4 ± 1.2	18.4 ± 2.2	6×10^{-6}
	10 CV cycles	$R_e(R_1Q_1)(R_2Q_2)Q_w$	13 ± 2	6.1 ± 2.2	19.1 ± 4.2	6×10^{-5}

[a]NLLS analyses carried out on the Nyquist plots displayed in Fig. 4 with a Boukamp software [55, 56] by exclusively accepting fits with χ^2 values of the order of 10^{-4} or lower. See the Experimental section and Table 1 for acronyms.

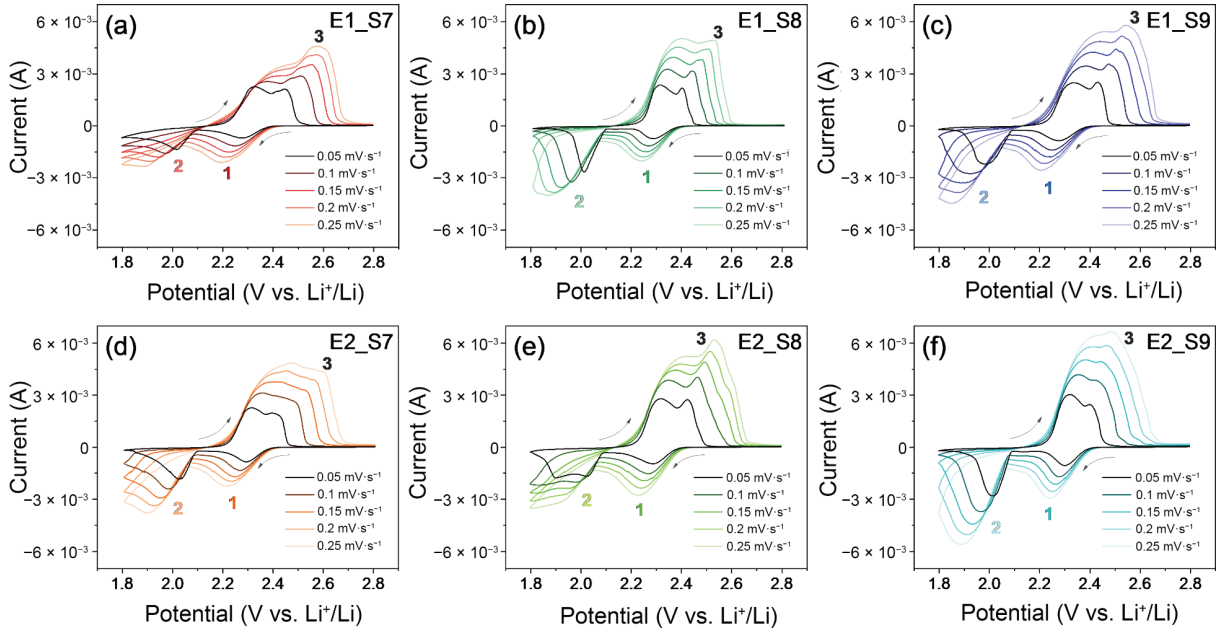

Figure 5 CV measurements related to Li|DOL:DME, 1 m LiTFSI, 1 m $LiNO_3$|S@SPC-73 cells with cathode formulations involving either ((a)–(c)) E1 or ((d)–(f)) E2 conductive agents and ((a) and (d)) S7, ((b) and (e)) S8, or ((c) and (f)) S9 carbon-coated Al current collectors (insets describe the cathode combinations). Voltammograms recorded at 0.05, 0.1, 0.15, 0.2, and 0.25 $mV \cdot s^{-1}$ increasing scan rates between 1.8 and 2.8 V vs. Li^+/Li. Cathode sulfur loading: 2 $mg \cdot cm^{-2}$ (electrode geometric area: 1.54 cm^2); E/S ratio: 15 $\mu L \cdot mg^{-1}$. The numbers in inset indicate the peak considered for the calculation of the D through Randles–Sevcik equation (Eq. (1)) [57, 58], see Figs. S3 and S4 in the ESM, and Table 5 for more details. Tests performed at room temperature (25 °C). See the Experimental section and Table 1 for acronyms.

in two charge plateaus centered at 2.3 and 2.4 V, in agreement with the voltammograms of Fig. 3. The voltage signatures also reveal a low polarization that hardly increases during the subsequent 150 runs, thus suggesting an optimized and efficient electrochemical process throughout the discharge/charge cycles taken into account. Further information is provided by the cycling trends in Figs. 6(b), 6(d), and 6(f) that allow a more detailed comparison of the various Li|S@SPC-73_E1 cells in terms of electrochemical stability. The tests indicate a first cycle capacity of 1130, 995, and 1058 $mAh \cdot g_S^{-1}$ for the S@SPC-73_E1 electrodes with either the S7 (Fig. 6(b)), S8 (Fig. 6(d)), or S9 (Fig. 6(f)) current collectors, respectively. The pristine capacity drastically decreases during the initial 40–50 cycles, and newly increases to stabilize at respective values of ~ 740 (Fig. 6(b)), ~ 700 (Fig. 6(d)), and ~ 810 $mAh \cdot g_S^{-1}$ (Fig. 6(f)). This behavior suggests a slow, but effective activation with consolidation of the electrode/electrolyte interphase, involving a partial loss of active material during the early stages of the test, subsequently leading to favorable structural rearrangements of the electrode structure, better electric contact of sulfur with the cathode, and enhancement of the cycling performance [39, 40]. Therefore, the initial capacity values can be hardly associated with the final capacity retention which is instead strongly influenced by the electrode composition. In turn, the activation ensures satisfactory steady state capacity values and a retention of 64%, 66%, and 73% with respect to the initial one upon 150 cycles (Figs. 6(b), 6(d), and 6(f), respectively). Moreover, the most relevant modification of the interphase is suggested to occur at the first cycle of the Li-S cells, during which the Coulombic efficiency in Figs. 6(b), 6(d), and 6(f) shows values exceeding 100% due to a partially irreversible discharge caused by side processes, in agreement with CV of Fig. 3. On the other hand, the cells subsequently operate with a satisfactory Coulombic efficiency that progressively reaches 97%.

The S@SPC-73_E2 electrodes were investigated by galvanostatic

Table 5 Estimation of the D^a

Electrode	State of charge (V vs. Li^+/Li)	D ($cm^2 \cdot s^{-1}$)
S@SPC-73_E1_S7	2.25 (during discharge, peak 1)	5.9×10^{-8}
	1.95 (during discharge, peak 2)	6.9×10^{-9}
	2.50 (during charge, peak 3)	2.1×10^{-8}
S@SPC-73_E1_S8	2.25 (during discharge, peak 1)	1.2×10^{-7}
	1.95 (during discharge, peak 2)	3.3×10^{-8}
	2.50 (during charge, peak 3)	6.3×10^{-8}
S@SPC-73_E1_S9	2.25 (during discharge, peak 1)	7.7×10^{-8}
	1.95 (during discharge, peak 2)	3.4×10^{-8}
	2.50 (during charge, peak 3)	3.7×10^{-8}
S@SPC-73_E2_S7	2.25 (during discharge, peak 1)	8.0×10^{-8}
	1.95 (during discharge, peak 2)	4.0×10^{-8}
	2.50 (during charge, peak 3)	3.6×10^{-8}
S@SPC-73_E2_S8	2.25 (during discharge, peak 1)	1.9×10^{-7}
	1.95 (during discharge, peak 2)	4.7×10^{-8}
	2.50 (during charge, peak 3)	8.6×10^{-8}
S@SPC-73_E2_S9	2.25 (during discharge, peak 1)	2.3×10^{-7}
	1.95 (during discharge, peak 2)	1.3×10^{-7}
	2.50 (during charge, peak 3)	1.1×10^{-7}

[a]*D* values calculated through Randles–Sevcik equation (Eq. (1)) [57, 58] by using the data collected in Fig. 5 and Fig. S3 in the ESM. Figure S4 in the ESM reports a graphical representation of the *D* values. See the Experimental section and Table 1 for acronyms.

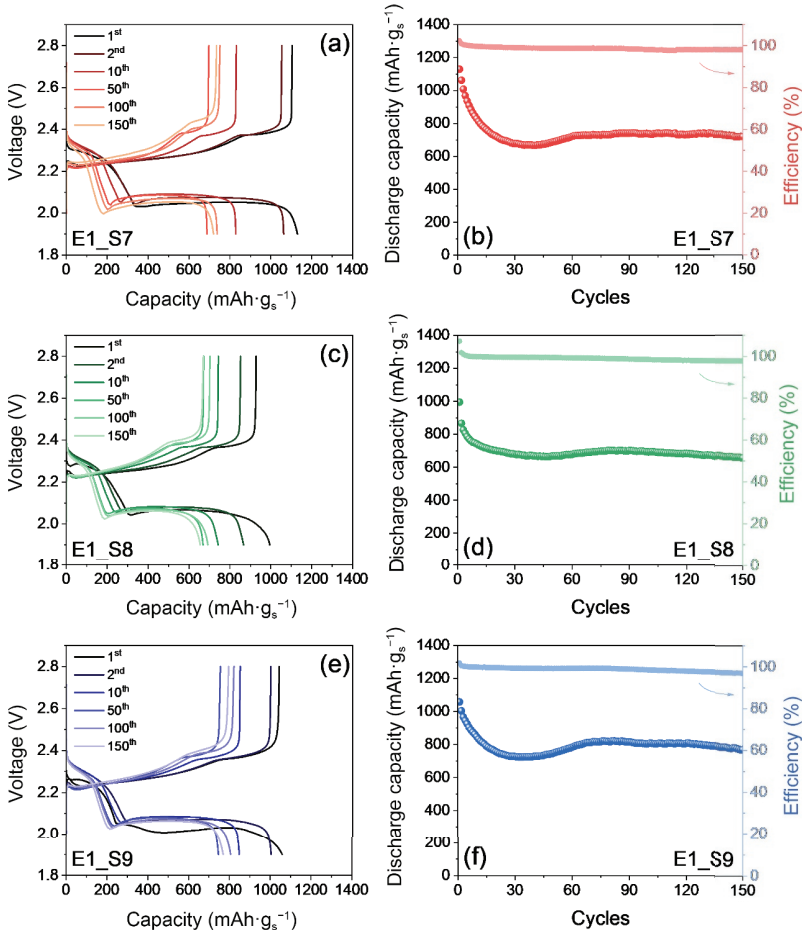

Figure 6 ((a), (c), and (e)) Voltage profiles and ((b), (d), and (f)) cycling trend (right *y*-axes show Coulombic efficiency) of galvanostatic tests performed on Li|DOL:DME, 1 m LiTFSI, 1 m $LiNO_3$|S@SPC-73_E1 cells with either the ((a) and (b)) S7, ((c) and (d)) S8, or ((e) and (f)) S9 carbon-coated Al current collectors (insets describe the various cathode combinations) at current rate of C/5 between 1.9 and 2.8 V. Sulfur loading: 1.5–2 mg·cm^{-2} (electrode geometric area: 1.54 cm^2); E/S ratio: 15 μL·mg^{-1}. Room temperature (25 °C). See the Experimental section and Table 1 for acronyms.

cycling in Fig. 7 using the same experimental setup previously adopted for the S@SPC-73_E1 ones. Hence, the voltage profiles of the Li|S@SPC-73_E2 cells using either S7 (Fig. 7(a)), S8 (Fig. 7(c)), or S9 (Fig. 7(e)) show the proper evolution of the reversible conversion of Li and S to lithium long-chain polysulfides at 2.3 and 2.1 V during discharge, and back to Li and S at 2.3 and 2.4 V during charge, with a low overvoltage in full agreement with the CV data of Fig. 4. Moreover, the cycling trends in Figs. 7(b), 7(d), and 7(f) reveal initial capacity values of 1129, 1067, and 999 mAh·g_S^{-1} for the cell using S7 (Fig. 7(b)), S8 (Fig. 7(d)), and S9 (Fig. 7(f)) supports, respectively, that decrease during the early stages of the test, increase afterwards to steady-state values of 780, 790, and 620 mAh·g_S^{-1}, and subsequently stabilize leading to a retention of 62%, 68%, and 62% with respect to the initial value after 150 cycles. As already observed for Li|S@SPC-73_E1 cells (Fig. 6), Li|S@SPC-73_E2 ones also show a slight irreversibility during the first cycle, while the final Coulombic efficiency notably approaches 98% upon 150 cycles.

In summary, both the Li|S@SPC-73_E1 (Fig. 6) and Li|S@SPC-73_E2 (Fig. 7) cells demonstrate promising cycling behavior depending on the carbon coating on the aluminum substrate. On the other hand, the data suggest the need for a careful tuning of the FLG loading when concomitantly used as electron conductor (E2) and as carbon coating on the aluminum substrate (S7 and S9). In fact, the advantages provided by this additive have been clearly evidenced by the mechanical stability and optimized morphology of the S@SPC-73_E2 electrode films (Fig. S2 in the ESM), and by the notable Li^+ diffusion properties exhibited in the S@SPC-73_E2_S9 electrode (Fig. S4 in the ESM and Table 5) which also shows a good overlapping of the galvanostatic profile (Fig. 7(e)) and the most enhanced stability of the electrochemical process (CV in Fig. 4(e)). Moreover, the cycling performance reported in Figs. 6 and 7 indicate that the use of FLG both as electron conductor and carbon coating agent may influence the capacity retention, as suggested by the trends related to the S@SPC-73_E2_S7 and S@SPC-73_E2_S9 electrodes (Figs. 7(b) and 7(f), respectively) which score the lowest retention of 62% with respect to the pristine value. In addition, the Li|S@SPC-73_E2_S9 cell shows the slowest capacity increase upon activation and exhibits the lowest final capacity after 150 cycles, i.e., 618 mAh·g_S^{-1}, while the other cells reach capacities between 660 and 770 mAh·g_S^{-1}. On the other hand, the use of FLG as the conductive agent and the MWCNTs as the carbon coating on Al in the S@SPC-73_E2_S8 electrode appears a suitable compromise for allowing optimal morphology, good mechanical stability, fast diffusion, high capacity values, and acceptable retention. The energy density of the each electrode is presented in Table S1 in the ESM with respect to the average voltage of 2.2 V (Figs. 6 and 7), the residual capacity value after 150 cycles (Table S2 in ESM), and the overall mass of the electrodes including the carbons, sulfur, and PVDF (Tables 1 and 2). The tables evidence that the electrodes S@SPC-73_E1_S9 and S@SPC-73_E2_S8 are characterized by the highest estimated energy values.

3.3 Investigation of the Li-S cells under challenging conditions

As mentioned during discussion of Figs. 6 and 7, a relatively low sulfur loading and high E/S ratio (i.e., 2 mg·cm^{-2} and 15 µL·mg_S^{-1}, respectively) were used to get the best performance of the studied materials, and to compare with Refs. [39, 40]. This aspect is further considered to achieve Li-S cells attaining practical

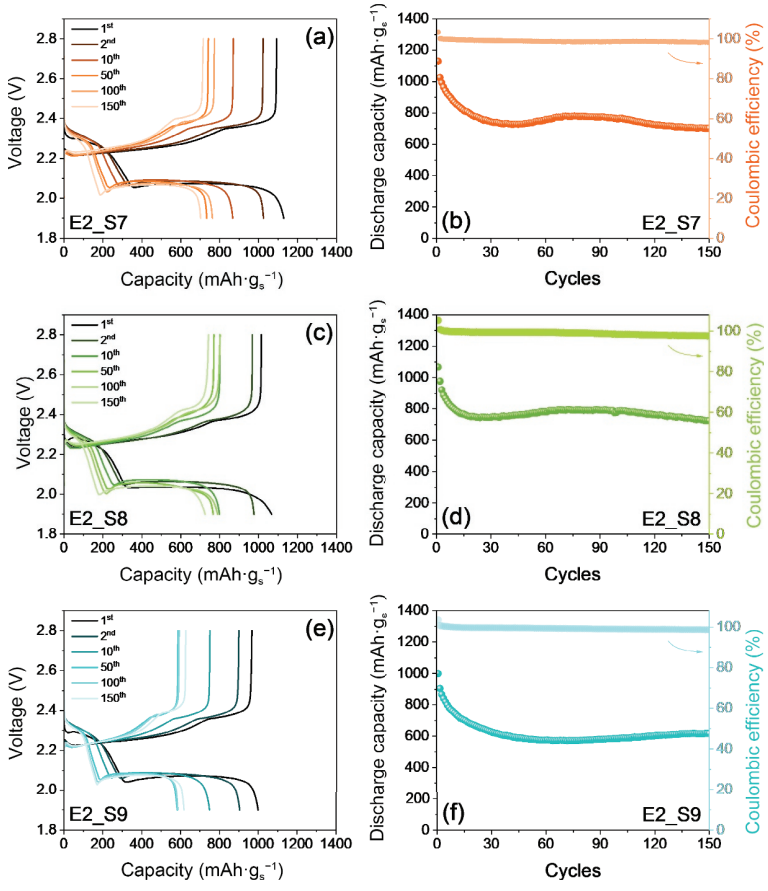

Figure 7 ((a), (c), and (e)) Voltage profiles and ((b), (d), and (f)) cycling trend (right *y*-axes show Coulombic efficiency) of galvanostatic tests performed on Li|DOL:DME, 1 m LiTFSI, 1 m $LiNO_3$|S@SPC-73_E2 cells with either the ((a) and (b)) S7, ((c) and (d)) S8, or ((e) and (f)) S9 carbon-coated Al current collectors (insets describe the various cathode combinations) at current rate of C/5 between 1.9 and 2.8 V. Sulfur loading: 1.5–2 mg·cm^{-2} (electrode geometric area: 1.54 cm^2); E/S ratio: 15 µL·mg^{-1}. Room temperature (25 °C). See the Experimental section and Table 1 for acronyms.

parameters by using increased sulfur loading on the cathode and limited E/S ratio, which are key parameters to achieve considerable energy density [69]. With the aim of evaluating the most promising Li-S system among the ones proposed herein, the S@SPC-73 electrodes are compared in terms of Li^+ diffusional properties and electrochemical performance in Li cell. In this regard, Figs. 8(a) and 8(b) show histograms representing the maximum D coefficient (D_{max} on the left y-axis, extracted from Table 5) and the residual capacity exhibited upon 150 discharge/charge cycles (right y-axis, obtained from Figs. 6 and 7) of S@SPC-73_E1 (Fig. 8(a)) and S@SPC-73_E2 (Fig. 8(b)) systems (Table S2 in the ESM reports the actual values of D_{max}, capacity, and corresponding retention). It is worth mentioning that the study of the Li^+ diffusional characteristics plays an essential role, particularly for challenging systems such as the Li-S battery which involves insulating species such as S and Li_2S in the electrode/electrolyte interphase. Therefore, the choice of the optimal support and electronic conductor is based herein on the maximum D value achieved by the electrodes as well as the capacity retention of the cells upon 150 cycles. The combination of these parameters represents in fact the most relevant indication on the effect of the current collector and conductive agent on the cell performances. Despite the S@SPC-73_E1_S9 electrode ensures the highest steady state capacity of 770 mAh·g_S^{-1} in lithium cell, the corresponding D_{max} is among the lowest ones, that is, 7.7×10^{-8} $cm^2 \cdot s^{-1}$ (Fig. 8(a) and Table 5). Instead, the S@SPC-73_E2_S8 and S@SPC-73_E2_S9 cathodes reveal the highest D_{max}, that is, 1.9×10^{-7} and 2.3×10^{-7} $cm^2 \cdot s^{-1}$, respectively, whilst only the E2_S8 combination ensures a considerable final capacity of 725 mAh·g^{-1} and a good retention of 68% with respect to the pristine value over 150 cycles (Fig. 8(b)). Moreover, the S@SPC-73_E2_S7 electrode has a D_{max} of 8.0×10^{-8} $cm^2 \cdot s^{-1}$ (Fig. 8(b)) which is far lower with respect to S@SPC-73_E2_S8 and S@SPC-73_E2_S9, likely due to the above mentioned excessive presence of FLG in the cathode formulation that can slow down the lithium ions diffusion at the electrode/electrolyte/interphase. Therefore, the S@SPC-73_E2_S8 cathode was selected among the various formulations for the additional cycling tests in lithium cell with sulfur loading increased to 5 mg·cm^{-2} and E/S ratio decreased to 10 μL·mg^{-1} at C/5 (Figs. 8(c) and 8(d)). A further test under more challenging condition is performed using the same electrode in a lithium cell with sulfur loading raised up to 6.5 mg·cm^{-2} and E/S ratio limited to 7 μL·mg^{-1} at C/10 (Figs. 8(e) and 8(f)). The related voltage profiles (Figs. 8(c) and 8(e)) show for both the measurements a relevant slope of the discharge plateaus evolving between 2.0 and 1.7 V at the first cycle, and suggest a partially hindered kinetics that greatly improve in the subsequent cycles by the ongoing of the activation [32].

Hence, the subsequent profiles display well defined double discharge plateaus between 2.3 and 1.9 V and merged charge steps evolving from 2.3 to 2.4 V ascribed to the reversible Li-S conversion process [63]. The corresponding capacity trends (Figs. 8(d) and 8(f)) well highlight the progressive enhancement of the

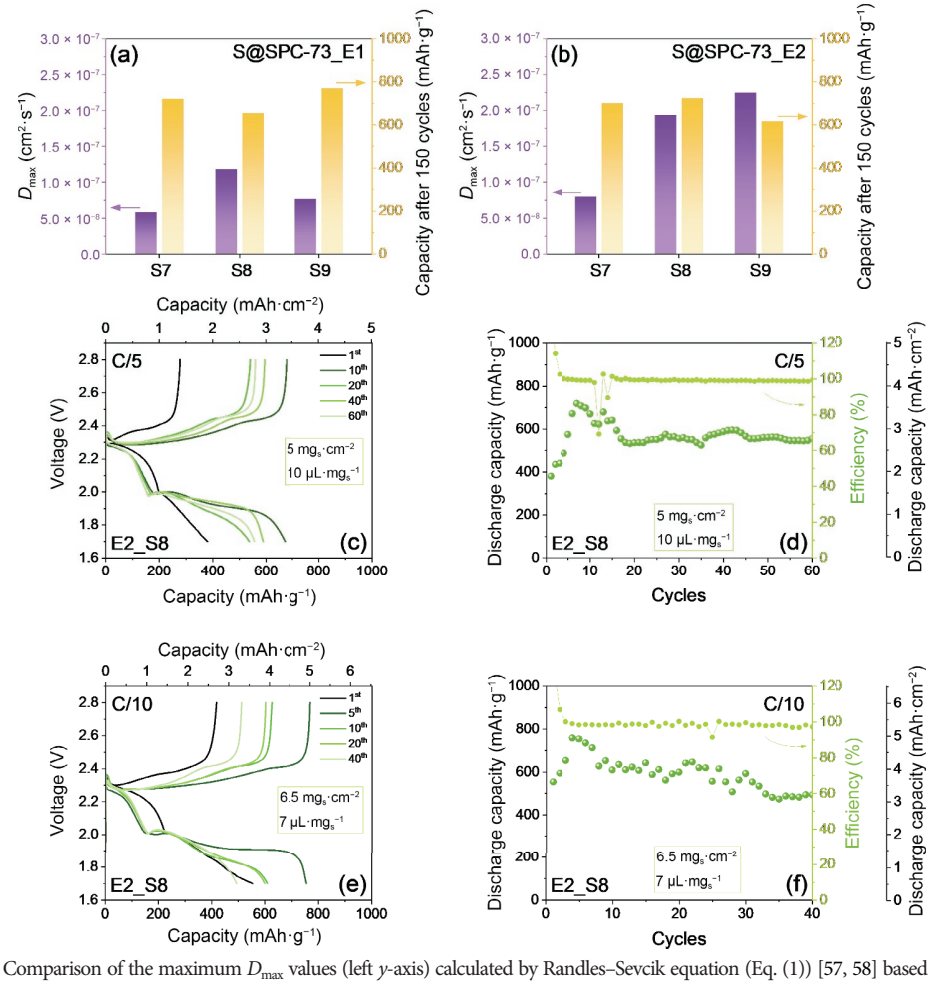

Figure 8 ((a) and (b)) Comparison of the maximum D_{max} values (left y-axis) calculated by Randles–Sevcik equation (Eq. (1)) [57, 58] based on the data of Fig. 5 and Table 5, and Figs. S3 and S4 in the ESM, and of the specific capacities (right y-axis) after 150 cycles at C/5 (see Figs. 6 and 7) of Li|DOL:DME, 1 m LiTFSI, and 1 m $LiNO_3$|S@SPC-73 cells with cathode formulations involving either (a) E1 or (b) E2 electron conductive agents and S7, S8, or S9 carbon-coated Al current collectors. The used data are reported in Table S2 in the ESM. ((c) and (e)) Voltage profiles and ((d) and (f)) cycling trends of Li|DOL:DME, 1 m LiTFSI, 1 m $LiNO_3$|S@SPC-73_E2_S8 cells cycled either ((c) and (d)) at C/5 with sulfur loading of 5 mg·cm^{-2} and E/S ratio of 10 μL·mg^{-1}, or ((e) and (f)) at C/10 with sulfur loading of 6.5 mg·cm^{-2} and E/S ratio of 7 μL·mg^{-1}. Top x-axis in ((c) and (e)) and additional right y-axis in ((d) and (f)) display the areal capacity in mAh·cm^{-2}. Electrode geometric area: 1.54 cm^2. Voltage range: 1.7–2.8 V. Tests performed at 30 °C. See the Experimental section and Table 1 for acronyms.

cycling behavior during the first 5–10 cycles as the discharge capacity increases from initial values of 380 mAh·g_S^{-1} at C/5 (Fig. 8(d)) and 550 mAh·g_S^{-1} at C/10 (Fig. 8(f)) to maximum values of 720 and 760 mAh·g_S^{-1}. At the end of the test, the cells cycled at C/5 and C/10 deliver capacities of 555 and 430 mAh·g_S^{-1}, with a retention of 77% and 65%, respectively, with respect to the maximum achieved values. It is worth mentioning that the activation trend observed herein greatly differs from the one observed in Figs. 6 and 7 for Li-S cells with sulfur loading approaching 2 mg·cm^{-2} and E/S ratio of 15 μL·mg^{-1}. This behavior is likely associated with the slow kinetics of the conversion process between Li and S during the initial stages of the test due to the demanding cell setup adopted in Fig. 8. On the other hand, both cells demonstrate a Coulombic efficiency approaching 99% after the first cycles, despite sporadic falls possibly ascribed to small dendrites or minor electrode detachment. Relevantly, the Li-S systems deliver promising areal capacities (additional right *y*-axes in Figs. 8(d) and 8(f)) referred to the geometric electrode area of 1.54 cm^2. Indeed, the cell cycled at C/5 has a maximum value of 3.6 mAh·cm^{-2} and approaches 3 mAh·cm^{-2} at the steady state, while values of ~ 5 and ~ 4 mAh·cm^{-2} are achieved at C/10, respectively. Therefore, the above tests suggest the Li-S cells with cathodes benefitting from FLG electron conductor and MWCNTs current collector coating as suitable materials even under practical operative conditions such as increased sulfur loading, limited E/S ratio, and thin layer configuration, which are certainly requested for boosting both the gravimetric and the volumetric energy densities, and finally scaling-up the battery [37]. Li-S pouch-cells can represent a scaled-up version of the system which can however involve other parameters that influence the cell performances rather than the ones investigated herein, mainly dealing with the cell geometry and assembly procedure [70]. Instead, in this work we focus the attention on the fundamental role of the current collector by comparing bare aluminum and a thin three-dimensional (3D) carbon-coated aluminum, which enhances the Li-S performance through increased porosity and avoid, at the same time, excessive thickness, and weight of the sulfur electrode [71, 72]. Practical aspects on scaled-up pouch cells certainly require further work aimed to achieve a high-performance battery [73], which is planned as future activity in our laboratories.

4 Conclusions

Current collectors using FLG, MWCNTs, or a mixture of them on aluminum were studied for application in Li-S battery. The morphology of the carbon-coated aluminum substrates was analyzed by SEM-EDS and TEM, which revealed an ordered flat surface for FLG, a rough and macroporous shape for MWCNTs, and an intermediate combination of these features for the FLG:MWCNTs mixture. Furthermore, XRD measurements suggested a relevant graphitic crystallinity, in particular for the support using the FLG as the only coating on Al. Electrodes were prepared using the carbon-coated current collectors, a sulfur-carbon black composite, and either SPC or FLG electron conductive agent to achieve six formulations with remarkable differences in terms of morphology. The electrodes using SPC conductive agent were characterized by a surface marked by micrometric cracks, strongly mitigated in the ones using FLG that guarantees enhanced mechanical stability of the film. CV tests performed on Li-S cells have shown fast and reversible conversion process for all the electrodes. Moreover, an activation of the electrode/electrolyte interphase, leading to the shift of the reduction peaks towards higher potential with consequent decrease of polarization, was observed upon the first CV and ascribed to the structural reorganization of the sulfur-carbon cathode and the formation of a suitable SEI. The EIS measurements performed upon CV confirmed the enhancement of the interphase properties, and displayed remarkable decrease of the associated resistance after the initial CV to low and stable values between 14 and 30 Ω, thus suggesting remarkable conductivity improvement of the Li-S systems. CV at increasing scan rate was used to estimate the *D* at various SOC. The data highlighted higher coefficients for the electrodes using FLG conductive agent compared to SPC, in particular in combination with MWCNTs in the Al-coating with a maximum *D* value as high as 2.3×10^{-7} $cm^2 \cdot s^{-1}$. On the other hand, the cathodes using FLG both as conductive agent and in the carbon coating exhibited the lowest capacity retention of 62% upon 150 cycles. Among the various electrodes, the one using FLG conductive agent and MWCNTs Al-coating has shown an initial capacity of ~ 1070 mAh·g_S^{-1} retained for over 68% at the end of the test, and a final Coulombic efficiency of 98%. Therefore, the electrode was selected for additional cycling tests with increased sulfur loading and limited E/S ratio to achieve practical values suitable for battery applications. The cells exhibited satisfactory capacity with maximum values of 720 mAh·g_S^{-1} at C/5 (5 mg·cm^{-2} and 10 μL·mg^{-1}) and 760 mAh·g_S^{-1} at C/10 (6.5 mg·cm^{-2} and 7 μL·mg^{-1}), corresponding to areal capacities of 3.6 and 5 mAh·cm^{-2}, respectively, retained for the 77% and 65% at the end of the tests. Therefore, the proper combination of FLG and MWCNTs in the sulfur electrode formulation may lead to stable and efficient cathodes suitable for achieving Li-S batteries of practical interest.

Acknowledgements

This project/work has received funding from the European Union's Horizon 2020 research and innovation programme Graphene Flagship (No. 881603). The authors also thank grant "Fondo di Ateneo per la Ricerca Locale (FAR) 2021", University of Ferrara, and the collaboration project "Accordo di Collaborazione Quadro 2015" between University of Ferrara (Department of Chemical and Pharmaceutical Sciences) and Sapienza University of Rome (Department of Chemistry).

Funding note: Open Access funding provided by Istituto Italiano di Tecnologia within the CRUI-CARE Agreement.

Electronic Supplementary Material: Supplementary Material (SEM-EDS measurements, linear fits of CV peak currents, and graphical representation of *D* coefficients) is available in the online version of this article at https://doi.org/10.1007/s12274-022-5364-5.

References

[1] Chung, S. H.; Chang, C. H.; Manthiram, A. Progress on the critical parameters for lithium-sulfur batteries to be practically viable. *Adv. Funct. Mater.* **2018**, *28*, 1801188.

[2] Carbone, L.; Greenbaum, S. G.; Hassoun, J. Lithium sulfur and lithium oxygen batteries: New frontiers of sustainable energy storage. *Sustain. Energy Fuels* **2017**, *1*, 228–247.

[3] Ji, X. L.; Lee, K. T.; Nazar, L. F. A highly ordered nanostructured carbon-sulphur cathode for lithium-sulphur batteries. *Nat. Mater.* **2009**, *8*, 500–506.

[4] Shin, H.; Baek, M.; Gupta, A.; Char, K.; Manthiram, A.; Choi, J. W. Recent progress in high donor electrolytes for lithium-sulfur batteries. *Adv. Energy Mater.* **2020**, *10*, 2001456.

[5] Zhang, S. G.; Ueno, K.; Dokko, K.; Watanabe, M. Recent advances in electrolytes for lithium-sulfur batteries. *Adv. Energy Mater.* **2015**, *5*, 1500117.

[6] Scrosati, B.; Hassoun, J.; Sun, Y. K. Lithium-ion batteries. A look into the future. *Energy Environ. Sci.* **2011**, *4*, 3287–3295.

[7] Xiao, J.; Hu, J. Z.; Chen, H. H.; Vijayakumar, M.; Zheng, J. M.; Pan, H. L.; Walter, E. D.; Hu, M.; Deng, X. C.; Feng, J. et al. Following the transient reactions in lithium-sulfur batteries using an *in situ* nuclear magnetic resonance technique. *Nano Lett.* **2015**, *15*, 3309–3316.

[8] Wang, Q.; Zheng, J. M.; Walter, E.; Pan, H. L.; Lv, D. P.; Zuo, P. J.; Chen, H. H.; Deng, Z. D.; Liaw, B. Y.; Yu, X. Q. et al. Direct observation of sulfur radicals as reaction media in lithium sulfur batteries. *J. Electrochem. Soc.* **2015**, *162*, A474–A478.

[9] Huang, Y. Z.; Lin, L.; Zhang, C. K.; Liu, L.; Li, Y. K.; Qiao, Z. S.; Lin, J.; Wei, Q. L.; Wang, L. S.; Xie, Q. S. et al. Recent advances and strategies toward polysulfides shuttle inhibition for high-performance Li-S batteries. *Adv. Sci.* **2022**, *9*, 2106004.

[10] Di Donato, G.; Ates, T.; Adenusi, H.; Varzi, A.; Navarra, M. A.; Passerini, S. Electrolyte measures to prevent polysulfide shuttle in lithium-sulfur batteries. *Batter. Supercaps* **2022**, *5*, e202200097.

[11] Manthiram, A.; Fu, Y. Z.; Chung, S. H.; Zu, C. X.; Su, Y. S. Rechargeable lithium-sulfur batteries. *Chem. Rev.* **2014**, *114*, 11751–11787.

[12] Liang, J.; Sun, Z. H.; Li, F.; Cheng, H. M. Carbon materials for Li-S batteries: Functional evolution and performance improvement. *Energy Storage Mater.* **2016**, *2*, 76–106.

[13] Shi, H. F.; Lv, W.; Zhang, C.; Wang, D. W.; Ling, G. W.; He, Y. B.; Kang, F. Y.; Yang, Q. H. Functional carbons remedy the shuttling of polysulfides in lithium-sulfur batteries: Confining, trapping, blocking, and breaking up. *Adv. Funct. Mater.* **2018**, *28*, 1800508.

[14] Tang, T. Y.; Hou, Y. L. Multifunctionality of carbon-based frameworks in lithium sulfur batteries. *Electrochem. Energy Rev.* **2018**, *1*, 403–432.

[15] Benítez, A.; Amaro-Gahete, J.; Chien, Y. C.; Caballero, Á.; Morales, J.; Brandell, D. Recent advances in lithium-sulfur batteries using biomass-derived carbons as sulfur host. *Renew. Sustain. Energy Rev.* **2022**, *154*, 111783.

[16] Wang, J.; Yang, J.; Xie, J.; Xu, N. A novel conductive polymer-sulfur composite cathode material for rechargeable lithium batteries. *Adv. Mater.* **2002**, *14*, 963–965.

[17] Li, W. Y.; Zhang, Q. F.; Zheng, G. Y.; Seh, Z. W.; Yao, H. B.; Cui, Y. Understanding the role of different conductive polymers in improving the nanostructured sulfur cathode performance. *Nano Lett.* **2013**, *13*, 5534–5540.

[18] Liu, Y.; Haridas, A. K.; Cho, K. K.; Lee, Y.; Ahn, J. H. Highly ordered mesoporous sulfurized polyacrylonitrile cathode material for high-rate lithium sulfur batteries. *J. Phys. Chem. C* **2017**, *121*, 26172–26179.

[19] Cheng, C. S.; Chung, S. H. Rational design of high-performance nickel-sulfur nanocomposites by the electroless plating method for electrochemical lithium-sulfur battery cathodes. *Batter. Supercaps* **2022**, *5*, e202100323.

[20] Cheng, C. S.; Chung, S. H. Nickel-plated sulfur nanocomposites for electrochemically stable high-loading sulfur cathodes in a lean-electrolyte lithium-sulfur cell. *Chem. Eng. J.* **2022**, *429*, 132257.

[21] Marangon, V.; Hassoun, J. Sulfur loaded by nanometric tin as a new electrode for high-performance lithium/sulfur batteries. *Energy Technol.* **2019**, *7*, 1900081.

[22] Park, J. S.; Kim, J. H.; Yang, S. J. Rational design of metal-organic framework-based-materials for advanced Li-S batteries. *Bull. Korean Chem. Soc.* **2021**, *42*, 148–158.

[23] Zheng, Y.; Zheng, S. S.; Xue, H. G.; Pang, H. Metal-organic frameworks for lithium-sulfur batteries. *J. Mater. Chem. A* **2019**, *7*, 3469–3491.

[24] de Haro, J.; Benítez, A.; Caballero, Á.; Morales, J. Revisiting the HKUST-1/S composite as an electrode for Li-S batteries: Inherent problems that hinder its performance. *Eur. J. Inorg. Chem.* **2021**, *2021*, 177–185.

[25] Marangon, V.; Scaduti, E.; Vinci, V. F.; Hassoun, J. Scalable composites benefiting from transition metal oxides as cathode materials for efficient lithium-sulfur batteries. *ChemElectroChem* **2022**, *9*, e202200374.

[26] Li, M. X.; Dai, Y.; Pei, X. M.; Chen, W. Hierarchically porous γ-Ti_3O_5 hollow nanospheres as an effective sulfur host for long-life lithium-sulfur batteries. *Appl. Surf. Sci.* **2022**, *579*, 152178.

[27] Liu, X.; Huang, J. Q.; Zhang, Q.; Mai, L. Q. Nanostructured metal oxides and sulfides for lithium-sulfur batteries. *Adv. Mater.* **2017**, *29*, 1601759.

[28] Di Lecce, D.; Marangon, V.; Jung, H. G.; Tominaga, Y.; Greenbaum, S.; Hassoun, J. Glyme-based electrolytes: Suitable solutions for next-generation lithium batteries. *Green Chem.* **2022**, *24*, 1021–1048.

[29] Zhang, S. G.; Ikoma, A.; Li, Z.; Ueno, K.; Ma, X. F.; Dokko, K.; Watanabe, M. Optimization of pore structure of cathodic carbon supports for solvate ionic liquid electrolytes based lithium-sulfur batteries. *ACS Appl. Mater. Interfaces* **2016**, *8*, 27803–27813.

[30] Marangon, V.; Minnetti, L.; Adami, M.; Barlini, A.; Hassoun, J. Lithium-metal batteries using sustainable electrolyte media and various cathode chemistries. *Energy Fuels* **2021**, *35*, 10284–10292.

[31] Santiago, A.; Castillo, J.; Garbayo, I.; de Buruaga, A. S.; Coca Clemente, J. A.; Qiao, L. X.; Cid Barreno, R.; Martinez-Ibañez, M.; Armand, M.; Zhang, H. et al. Salt additives for improving cyclability of polymer-based all-solid-state lithium-sulfur batteries. *ACS Appl. Energy Mater.* **2021**, *4*, 4459–4464.

[32] Marangon, V.; Di Lecce, D.; Minnetti, L.; Hassoun, J. Novel lithium-sulfur polymer battery operating at moderate temperature. *ChemElectroChem* **2021**, *8*, 3971–3981.

[33] Zhang, Q.; Huang, N.; Huang, Z.; Cai, L. T.; Wu, J. H.; Yao, X. Y. CNTs@S composite as cathode for all-solid-state lithium-sulfur batteries with ultralong cycle life. *J. Energy Chem.* **2020**, *40*, 151–155.

[34] Zhang, H.; Eshetu, G. G.; Judez, X.; Li, C. M.; Rodriguez-Martínez, L. M.; Armand, M. Electrolyte additives for lithium metal anodes and rechargeable lithium metal batteries: Progress and perspectives. *Angew. Chem., Int. Edit.* **2018**, *57*, 15002–15027.

[35] Rosenman, A.; Elazari, R.; Salitra, G.; Markevich, E.; Aurbach, D.; Garsuch, A. The effect of interactions and reduction products of $LiNO_3$, the anti-shuttle agent, in Li-S battery systems. *J. Electrochem. Soc.* **2015**, *162*, A470–A473.

[36] Xiong, S. Z.; Xie, K.; Diao, Y.; Hong, X. B. Characterization of the solid electrolyte interphase on lithium anode for preventing the shuttle mechanism in lithium-sulfur batteries. *J. Power Sources* **2014**, *246*, 840–845.

[37] Bhargav, A.; He, J. R.; Gupta, A.; Manthiram, A. Lithium-sulfur batteries: Attaining the critical metrics. *Joule* **2020**, *4*, 285–291.

[38] Dörfler, S.; Althues, H.; Härtel, P.; Abendroth, T.; Schumm, B.; Kaskel, S. Challenges and key parameters of lithium-sulfur batteries on pouch cell level. *Joule* **2020**, *4*, 539–554.

[39] Marangon, V.; Di Lecce, D.; Orsatti, F.; Brett, D. J. L.; Shearing, P. R.; Hassoun, J. Investigating high-performance sulfur-metal nanocomposites for lithium batteries. *Sustain. Energy Fuels* **2020**, *4*, 2907–2923.

[40] Marangon, V.; Di Lecce, D.; Brett, D. J. L.; Shearing, P. R.; Hassoun, J. Characteristics of a gold-doped electrode for application in high-performance lithium-sulfur battery. *J. Energy Chem.* **2022**, *64*, 116–128.

[41] Benítez, A.; Caballero, Á.; Rodríguez-Castellón, E.; Morales, J.;

Hassoun, J. The role of current collector in enabling the high performance of Li/S battery. *ChemistrySelect* **2018**, *3*, 10371–10377.
[42] Benítez, A.; Luna-Lama, F.; Caballero, A.; Rodríguez-Castellón, E.; Morales, J. Contribution to the understanding of the performance differences between commercial current collectors in Li-S batteries. *J. Energy Chem.* **2021**, *62*, 295–306.
[43] Brehm, W.; Marangon, V.; Panda, J.; Thorat, S. B.; del Rio Castillo, A. E.; Bonaccorso, F.; Pellegrini, V.; Hassoun, J. A lithium-sulfur battery using binder-free graphene-coated aluminum current collector. *Energy Fuels* **2022**, *36*, 9321–9328.
[44] Bonaccorso, F.; Colombo, L.; Yu, G. H.; Stoller, M.; Tozzini, V.; Ferrari, A. C.; Ruoff, R. S.; Pellegrini, V. Graphene, related two-dimensional crystals, and hybrid systems for energy conversion and storage. *Science* **2015**, *347*, 1246501.
[45] Fiori, G.; Bonaccorso, F.; Iannaccone, G.; Palacios, T.; Neumaier, D.; Seabaugh, A.; Banerjee, S. K.; Colombo, L. Electronics based on two-dimensional materials. *Nat. Nanotechnol.* **2014**, *9*, 768–779.
[46] Carbone, L.; Del Rio Castillo, A. E.; Panda, J. K.; Pugliese, G.; Scarpellini, A.; Bonaccorso, F.; Pellegrini, V. High-sulfur-content graphene-based composite through ethanol evaporation for high-energy lithium-sulfur battery. *ChemSusChem* **2020**, *13*, 1593–1602.
[47] Del Rio Castillo, A. E.; Ansaldo, A.; Pellegrini, V.; Bonaccorso, F. Exfoliation of layered materials by wet-jet milling techniques. U. S. Patent 10, 407, 308, September 10, 2019.
[48] Del Rio Castillo, A. E.; Pellegrini, V.; Ansaldo, A.; Ricciardella, F.; Sun, H.; Marasco, L.; Buha, J.; Dang, Z.; Gagliani, L.; Lago, E. et al. High-yield production of 2D crystals by wet-jet milling. *Mater. Horiz.* **2018**, *5*, 890–904.
[49] Venezia, E.; Carbone, L.; Bonaccorso, F.; Pellegrini, V. Tuning the morphology of sulfur-few layer graphene composites via liquid phase evaporation for battery application. *Nanoscale Adv.* **2022**, *4*, 1136–1144.
[50] Su, Y. S.; Fu, Y. Z.; Manthiram, A. Self-weaving sulfur-carbon composite cathodes for high rate lithium-sulfur batteries. *Phys. Chem. Chem. Phys.* **2012**, *14*, 14495–14499.
[51] Carbone, L.; Coneglian, T.; Gobet, M.; Munoz, S.; Devany, M.; Greenbaum, S.; Hassoun, J. A simple approach for making a viable, safe, and high-performances lithium-sulfur battery. *J. Power Sources* **2018**, *377*, 26–35.
[52] Zhu, L.; Peng, H. J.; Liang, J. Y.; Huang, J. Q.; Chen, C. M.; Guo, X. F.; Zhu, W. C.; Li, P.; Zhang, Q. Interconnected carbon nanotube/graphene nanosphere scaffolds as free-standing paper electrode for high-rate and ultra-stable lithium-sulfur batteries. *Nano Energy* **2015**, *11*, 746–755.
[53] Zhai, P. Y.; Huang, J. Q.; Zhu, L.; Shi, J. L.; Zhu, W. C.; Zhang, Q. Calendering of free-standing electrode for lithium-sulfur batteries with high volumetric energy density. *Carbon* **2017**, *111*, 493–501.
[54] Di Lecce, D.; Marangon, V.; Du, W. J.; Brett, D. J. L.; Shearing, P. R.; Hassoun, J. The role of synthesis pathway on the microstructural characteristics of sulfur-carbon composites: X-ray imaging and electrochemistry in lithium battery. *J. Power Sources* **2020**, *472*, 228424.
[55] Boukamp, B. A. A package for impedance/admittance data analysis. *Solid State Ion.* **1986**, *18–19*, 136–140.
[56] Boukamp, B. A. A nonlinear least squares fit procedure for analysis of immittance data of electrochemical systems. *Solid State Ion.* **1986**, *20*, 31–44.
[57] Randles, J. E. B. A cathode ray polarograph. Part II.—The current–voltage curves. *Trans. Faraday Soc.* **1948**, *44*, 327–338.
[58] Ševčík, A. Oscillographic polarography with periodical triangular voltage. *Collect. Czech. Chem. Commun.* **1948**, *13*, 349–377.
[59] Zhou, G. M.; Zhao, Y. B.; Manthiram, A. Dual-confined flexible sulfur cathodes encapsulated in nitrogen-doped double-shelled hollow carbon spheres and wrapped with graphene for Li-S batteries. *Adv. Energy Mater.* **2015**, *5*, 1402263.
[60] Yuan, Z.; Peng, H. J.; Huang, J. Q.; Liu, X. Y.; Wang, D. W.; Cheng, X. B.; Zhang, Q. Hierarchical free-standing carbon-nanotube paper electrodes with ultrahigh sulfur-loading for lithium-sulfur batteries. *Adv. Funct. Mater.* **2014**, *24*, 6105–6112.
[61] Zhang, Y. Y.; Gao, Z.; Song, N. N.; He, J. J.; Li, X. D. Graphene and its derivatives in lithium-sulfur batteries. *Mater. Today Energy* **2018**, *9*, 319–335.
[62] Shi, H. D.; Zhao, X. J.; Wu, Z. S.; Dong, Y. F.; Lu, P. F.; Chen, J.; Ren, W. C.; Cheng, H. M.; Bao, X. H. Free-standing integrated cathode derived from 3D graphene/carbon nanotube aerogels serving as binder-free sulfur host and interlayer for ultrahigh volumetric-energy-density lithium-sulfur batteries. *Nano Energy* **2019**, *60*, 743–751.
[63] Li, G. R.; Wang, S.; Zhang, Y. N.; Li, M.; Chen, Z. W.; Lu, J. Revisiting the role of polysulfides in lithium-sulfur batteries. *Adv. Mater.* **2018**, *30*, 1705590.
[64] Strubel, P.; Thieme, S.; Weller, C.; Althues, H.; Kaskel, S. Insights into the redistribution of sulfur species during cycling in lithium-sulfur batteries using physisorption methods. *Nano Energy* **2017**, *34*, 437–441.
[65] Tan, C.; Heenan, T. M. M.; Ziesche, R. F.; Daemi, S. R.; Hack, J.; Maier, M.; Marathe, S.; Rau, C.; Brett, D. J. L.; Shearing, P. R. Four-dimensional studies of morphology evolution in lithium-sulfur batteries. *ACS Appl. Energy Mater.* **2018**, *1*, 5090–5100.
[66] Aurbach, D. Review of selected electrode-solution interactions which determine the performance of Li and Li ion batteries. *J. Power Sources* **2000**, *89*, 206–218.
[67] Benítez, A.; Di Lecce, D.; Caballero, Á.; Morales, J.; Rodríguez-Castellón, E.; Hassoun, J. Lithium sulfur battery exploiting material design and electrolyte chemistry: 3D graphene framework and diglyme solution. *J. Power Sources* **2018**, *397*, 102–112.
[68] Benítez, A.; Marangon, V.; Hernández-Rentero, C.; Caballero, Á.; Morales, J.; Hassoun, J. Porous Cr_2O_3@C composite derived from metal organic framework in efficient semi-liquid lithium-sulfur battery. *Mater. Chem. Phys.* **2020**, *255*, 123484.
[69] Hagen, M.; Fanz, P.; Tübke, J. Cell energy density and electrolyte/sulfur ratio in Li-S cells. *J. Power Sources* **2014**, *264*, 30–34.
[70] Jiménez-Martín, G.; Castillo, J.; Judez, X.; Gómez-Urbano, J. L.; Moreno-Fernández, G.; Santiago, A.; de Buruaga, A. S.; Garbayo, I.; Coca-Clemente, J. A.; Villaverde, A. et al. Graphene-based activated carbon composites for high performance lithium-sulfur batteries. *Batter. Supercaps* **2022**, *5*, e202200167.
[71] Kim, H.; Lee, J. T.; Yushin, G. High temperature stabilization of lithium-sulfur cells with carbon nanotube current collector. *J. Power Sources* **2013**, *226*, 256–265.
[72] Peng, H. J.; Xu, W. T.; Zhu, L.; Wang, D. W.; Huang, J. Q.; Cheng, X. B.; Yuan, Z.; Wei, F.; Zhang, Q. 3D carbonaceous current collectors: The origin of enhanced cycling stability for high-sulfur-loading lithium-sulfur batteries. *Adv. Funct. Mater.* **2016**, *26*, 6351–6358.
[73] Cheng, Q.; Chen, Z. X.; Li, X. Y.; Hou, L. P.; Bi, C. X.; Zhang, X. Q.; Huang, J. Q.; Li, B. Q. Constructing a 700 $Wh{\cdot}kg^{-1}$-level rechargeable lithium-sulfur pouch cell. *J. Energy Chem.* **2023**, *76*, 181–186.